



SCHOOL OF COMPUTATION, INFORMATION AND  
TECHNOLOGY - INFORMATICS

TECHNISCHE UNIVERSITÄT MÜNCHEN

Master's Thesis in Biomedical Computing

**Deep Learning Based Analysis of  
Tumor-infiltrating Lymphocytes in H&E  
Stained Histological Sections for Survival  
Prediction of Breast Cancer patients**

**Margaryta Olenchuk**





SCHOOL OF COMPUTATION, INFORMATION AND  
TECHNOLOGY - INFORMATICS

TECHNISCHE UNIVERSITÄT MÜNCHEN

Master's Thesis in Biomedical Computing

**Deep Learning Based Analysis of  
Tumor-infiltrating Lymphocytes in H&E  
Stained Histological Sections for Survival  
Prediction of Breast Cancer patients**

**Deep Learning basierte Analyse von  
tumorinfiltrierenden Lymphozyten in H&E  
gefärbten histologischen Schnitten zur  
Überlebensvorhersage von  
Brustkrebspatienten**

Author:

Margaryta Olenchuk

Supervisor:

Prof. Dr. Peter Schüffler

Advisor:

Dr. Philipp Wortmann, Ansh Kapil

Submission Date:

15.12.2022

I confirm that this master's thesis in biomedical computing is my own work and I have documented all sources and material used.

Munich, 15.12.2022

Margaryta Olenchuk

## Acknowledgments

# **Abstract**

# **Kurzfassung**

# Contents

<b>Acknowledgments</b>	iii
<b>Abstract</b>	iv
<b>Kurzfassung</b>	v
<b>1 Introduction</b>	1
<b>2 Related work</b>	4
2.1 Deep learning-based semantic segmentation . . . . .	4
2.1.1 Fully convolutional networks (FCNs) . . . . .	4
2.1.2 Encoder-decoder networks . . . . .	4
2.1.3 Recurrent neural networks (RNNs) . . . . .	5
2.1.4 Transformers . . . . .	6
2.2 TILs as prognostic biomarker . . . . .	6
<b>3 Methods</b>	9
3.1 Semantic segmentation . . . . .	9
3.1.1 DeepLab . . . . .	9
3.1.2 Transformers . . . . .	11
3.1.3 TILs segmentation postprocessing . . . . .	14
3.2 Survival Analysis . . . . .	15
3.2.1 Kaplan–Meier estimator . . . . .	16
3.2.2 Cox model . . . . .	16
<b>4 Data</b>	19
4.1 Segmentation . . . . .	19
4.2 Survival Analysis . . . . .	21
<b>5 Results &amp; Discussion</b>	22
5.1 Tissue Segmentation . . . . .	22
5.2 TILs Segmentation . . . . .	30
5.3 Survival Analysis . . . . .	35
<b>6 Conclusion</b>	41
<b>List of Figures</b>	43

*Contents*

---

<b>List of Tables</b>	<b>45</b>
<b>Bibliography</b>	<b>46</b>

# 1 Introduction

Breast cancer is the most common form of cancer diagnosed worldwide and the leading cause of cancer-related death among women. [1] It is a heterogeneous disease, consisting of several morphological and molecular subtypes. The molecular subtypes are among the prime factors to characterize breast cancer. There are four main clinically used [2] groups defined based on the status of several receptors, namely the Hormonal Receptor (HR, which is positive if either Estrogen Receptor (ER) or Progesterone Receptor (PR) is positive) and the human epidermal growth factor receptor 2 (Her2):

1. Luminal A (HR positive, Her2 negative)
2. Luminal B (HR positive, Her2 positive)
3. Her2 enriched (HR negative, Her2 positive)
4. Triple Negative (HR negative, Her2 negative)

Regardless of the subtype, breast cancer is primarily classified by its histological appearance. Thus for diagnostic confirmation a patient's biopsy or surgical resection samples are sectioned onto microscope slides for staining, often with hematoxylin and eosin (H&E), followed by a visual diagnosis by a pathologist. Pathologists examine tissue for abnormalities that indicate breast cancer. Cancer causes changes in tissue at the sub-cellular scale, hence an analysis of normal and tumor tissue can provide novel insights into tissue characteristics, lead to a better understanding of mechanisms underlying cancer progression and provide valuable information for medical decision-making such as tumor grading and treatment choices. [3]

One of the characteristics of histological images that can be visually assessed by pathologists is lymphocytic infiltration. There are a number of publications that emphasize the prognostic value of tumor-infiltrating lymphocytes (TILs), especially in triple negative (TNBC) and human epidermal growth factor receptor 2 (HER2+) breast cancer [4, 5]. TILs are mononuclear immune cells that infiltrate tumor tissue. They have been detected in almost all solid tumors, including breast cancer. [6] The development and progression of malignant tumors can be characterized by an interaction between the cells in the tumor microenvironment and TILs. In the early stage HER2+ and TNBC, TILs are detectable in up to 75% of tumors. [7] Studies have shown that an increased degree of lymphocytic infiltration is predictive of better long-term control of the disease. The patients with a high proportion of TILs in the tumor tissue and high immunogenicity of the tumor were shown to respond better to the chemotherapy. Accumulating evidence indicates that tumor-infiltrating lymphocytes are clinically useful biomarkers in TNBC and HER2+ and that they play an essential role in cancer progression. [8] Further research and development of TILs related biomarkers would grant clinicians essential prognostic information and promote the research on novel treatments and therapeutics.

For instance, since TILs with exhausted phenotype are associated with loss of antitumor immunity, single-cell RNA-seq of TILs has been already performed to search for new immune checkpoint blockade targets that enable the precise definition and even novel development of therapeutic strategies to overcome T-cell exhaustion. Therapeutic approaches to influence T-cell exhaustion have been developed to target proteins CTLA-4, PD-1, and PD-L1 and have proven to be effective in treating melanoma and non-small-cell lung cancer during ongoing trials. [9] TILs in TNBC patients also display immuno-suppressive phenotypes [10] and the number of TILs detected by TNBC patients is one of the highest of all breast cancer subgroups [11] which makes TNBC a valid target for further TILs research.

A valuable contribution to TILs research and any task involving visual analysis of histological images would be method automatization. Because while the manual examination continues to be widely applied in a clinical setting, it is subjective and not scalable to translational and clinical research studies involving large datasets of high-resolution whole slide tissue images (WSIs). Hence, there is a raised demand for reliable and efficient automated methods to complement the traditional manual examination of tissue samples.

With advancing technology and access to a large amount of data, deep learning methods have garnered an interest in computational pathology. There are multiple deep learning-based methods and pipelines that have been proposed for detection and segmentation tasks of WSIs. To stimulate the development of algorithms for automatic TILs evaluation, a special Tumor InfiltratinG lymphocytes in breast cancER (TiGER) [12] challenge was formed. Within this competition, various algorithms were evaluated for the automated assessment of TILs in H&E stained histopathology WSIs that resulted in automatically acquired TILs scores. Those were later internally checked for significance as prognostic values and the concordnace was reported. The clinical focus of the TiGER challenge is on Her2+ and TNBC. It is motivated by research and clinical data that show that Her2+ and TNBC have the worst prognosis making them an intense target of prognostic and predictive biomarker research aimed at improving patient management and prognosis.

This work is closely linked to the TiGER challenge. The goal is to develop a pipeline for HER2 positive and triple negative breast cancer H&E slides that segments tumor and stroma regions, detects TILs, and produces TILs scores as pictured in Figure 1.1 block 1-3.

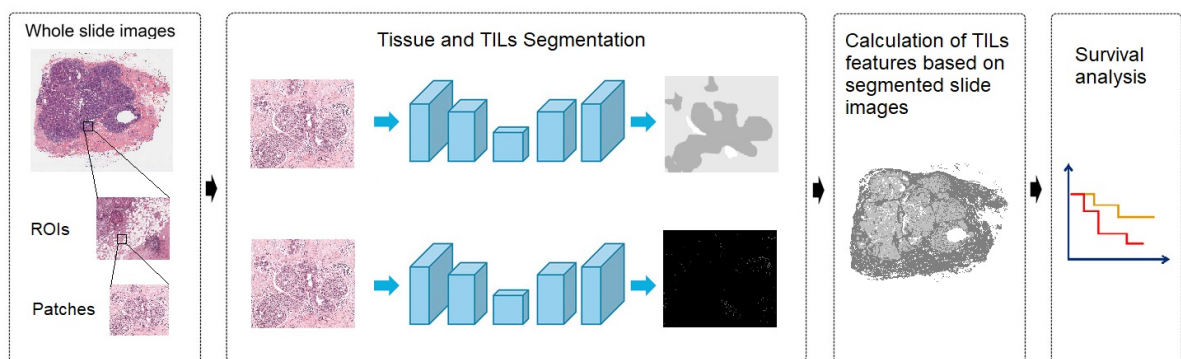


Figure 1.1: Abstract scheme to visually introduce the flow of this thesis work.

---

## *1 Introduction*

---

This work takes benefit of the annotated ROIs provided by the TiGER challenge for the development of patch-based automated tissue and TILs segmentation. As a step beyond the challenge, the scores based on the degree of lymphocytic infiltration are evaluated on the breast cancer TCGA-BRCA dataset generated by the TCGA Research Network and not on the hidden TiGER dataset which is not available after the end of the competition. The TCGA-BRCA clinical data enables independent broad survival analysis of different experimental TILs characteristics that can be calculated solely based on histological images (Figure 1.1 block 4). As a result, this work aims not only to develop a computational approach to compute TILs score on H&E images of Her2+ and TNBC but also experiment with different TILs scores and show detailed survival analysis based on publically available TCGA-BRCA dataset together with their predictive value for overall patient survival.

## 2 Related work

### 2.1 Deep learning-based semantic segmentation

The goal of semantic segmentation is to assign each image pixel to a category label corresponding to the underlying object. Due to the success of deep learning models in a wide range of vision applications, various deep learning-based algorithms have been developed and published in the literature [13]. One of the most prominent deep learning architectures used by the computer vision community include fully convolutional networks (FCNs) [14], encoder-decoders [15], generative adversarial networks (GANs) [16] and recurrent neural networks (RNNs) [17]. As tissue segmentation, TILs detection can also be viewed as a semantic segmentation problem, since detection bounding boxes can be transformed into pseudo-segmentation masks. The focus of the following chapters is to superficially introduce the existing deep learning-based approaches for the histopathological tasks, that can be adapted or extended for tissue and TILs segmentation of breast cancer WSIs.

#### 2.1.1 Fully convolutional networks (FCNs)

FCNs [14] are among the most widely used architectures for computer vision tasks and their general architecture consists of several learnable convolutions, pooling layers, and a final  $1 \times 1$  convolution. Such models are used on segmentation problems in histology domain such as colon glands segmentation [18], as well as nuclei [19] and TILs [20] segmentation for breast cancer all performed on the Hematoxylin and Eosin (H&E) stained histopathology images. Moreover, the FCN method was applied for semantic segmentation of TCGA [21] breast data set [22], which is also used in this thesis. However, despite its popularity, the conventional FCN model has limitations such as loss of localization and the inability to process potentially useful global context information due to a series of down-sampling and a high sampling rate.

#### 2.1.2 Encoder-decoder networks

A popular group of deep learning models for semantic image segmentation that aims to solve the aforementioned issues of FCNs is based on the convolutional encoder-decoder architecture [15]. Their model consists of two parts, an encoder consisting of convolutional layers and a deconvolution network that consists of deconvolution and unpooling layers that take the feature vector as input and generate a map of pixel-wise class probabilities. An example of such a convolutional encoder-decoder architecture for image segmentation is SegNet [23]. The SegNet's encoder network has 13 convolutional layers with corresponding layers in the decoder. The final decoder output is fed to a multi-class soft-max classifier to

produce class probabilities for each pixel independently. The main feature of SegNet is that the decoder uses pooling indices computed in the max-pooling step of the corresponding encoder to perform non-linear upsampling. This architecture also find a use in histopathology, e.g. colon cancer analysis [24]. There are several encoder-decoder models initially developed for biomedical image segmentation. Ronneberger et al. [25] proposed the U-Net model for segmenting biological microscopy images that can train with few annotated images effectively. U-Net has an FCN-like down-sampling part that extracts features with  $3 \times 3$  convolutions and an up-sampling part. Feature maps from the encoder are copied to the corresponding decoder part of the network to avoid losing pattern information. Besides the segmentation of neuronal structures in electron microscopic recordings demonstrated in the original paper [25], U-Net was applied for numerous histopathology tasks such as nuclei segmentation [26, 27], individual colon glands segmentation [28], epidermal tissue segmentation of skin biopsies [29] and cell segmentation on triple-negative breast cancer patients dataset [30]. A further development of an encoder-decoder model for semantic segmentation of histopathology images is HookNet [31]. The architecture consists of two encoder-decoder branches to extract contextual and fine-grained detailed information and combine it (hook up) for the target segmentation. The model showed improvement compared with single-resolution models and was applied to segment breast cancer tissue sections [31].

Another widely used group of deep learning models for semantic segmentation are the atrous (or dilated) convolutional models that include the DeepLab family [32, 33]. The use of atrous convolutions addresses the decreasing resolution caused by max-pooling and striding and Atrous Spatial Pyramid Pooling analyzes an incoming convolutional feature layer with filters at multiple sampling rates allowing to capture objects and image contexts at multiple scales to robustly segment objects at multiple scales. DeepLabv3+ [34] uses encoder-decoder architecture including atrous separable convolution, composed of a depthwise convolution (spatial convolution for each channel of the input) and pointwise convolution ( $1 \times 1$  convolution with the depthwise convolution as input). Authors [34] demonstrated the effectiveness of DeepLabv3+ model on segmentation of H&E stained breast cancer [35]. Despite all the efforts, even this popular architecture has constraints in learning long-range dependency and spatial correlations due to the inductive bias of locality and weight sharing [36] that may result in the sub-optimal segmentation of complex structures.

### 2.1.3 Recurrent neural networks (RNNs)

RNNs [17] have proven to be useful in modeling the short/long-term dependencies among pixels to generate segmentation maps. Pixels can be linked together and processed sequentially to model global contexts and improve semantic segmentation. ReSeg [37] is an RNN-based model for semantic segmentation. Each layer is composed of four RNNs that go through the image horizontally and vertically in both directions to provide relevant global information, while convolutional layers extract local features that are then followed by up-sampling layers to recover the predictions at original image resolution. But despite all further developments that showcase the potential for histopathology image segmentation: RACE-net [38] applied for segmentation of the cell nuclei in H&E stained breast cancer slides,

Her2Net [39] segmenting cell membranes and nuclei from human epidermal growth factor receptor-2 (HER2)-stained breast cancer images, etc., an important limitation of RNNs is that, due to their sequential nature, they are comparably slower, since this sequential calculation cannot be easily parallelized.

#### 2.1.4 Transformers

The Transformer in Natural Language Processing is an architecture that aims to solve sequence-to-sequence problems. These models rely on self-attention mechanisms and capture long-range dependencies among tokens (words) in a sentence without using RNNs or convolution. Transformers have also emerged in image semantic segmentation. Recent studies have shown that the Transformers can achieve superior performance than CNN-based approaches in various semantic segmentation applications [40]. The state-of-the-art Transformer-based semantic segmentation methods can be often applied either as convolution-free models or/and as CNN-Transformer hybrid models. Swin-Transformer [41] for instance is a pure hierarchical Transformer that can serve as a backbone for various computer vision tasks including semantic segmentation. To tokenize the image, it brakes the image into windows that further consist of patches. It constructs a hierarchical representation of an image by starting from small-sized patches and gradually merging neighboring patches into deeper Transformer layers. Swin-Transformer or its slightly modified successors found its application in the medical domain, often as a backbone, for example for colon cancer segmentation in H&E stained histopathology images [42] or gland segmentation [43]. A further popular fully transformer-based model for semantic segmentation is Segmenter [44]. The encoder consists of Multi-head Self Attention and Multi-Layer Perceptron (MLP) blocks, as well as two-layer norms and residual connections after each block and a linear decoder that bilinearly up-samples the sequence into a 2D segmentation mask. While performing well on scene segmentation [44], is not particularly used in the medical domain. In the field of medical image segmentation, TransUNet [45] was the first attempt to establish self-attention mechanisms by combining transformer with U-Net and proved that transformers can be used as powerful encoders for medical image segmentation. A novel positional-encoding-free Transformer SegFormer [46] set new state-of-the-art in terms of efficiency and accuracy in publicly available semantic segmentation datasets and applied for gland and nuclei segmentation [43]. This architecture remains promising also for semantic segmentation in medical applications due to the positional-encoding-free encoder and lightweight MLP decoder.

## 2.2 TILs as prognostic biomarker

The overall survival (OS) is the primary endpoint for prognostic analysis in this thesis, the survival methods are well established and include the Kaplan–Meier method [47] to estimate OS and Cox proportional hazard models [48] to quantify the hazard ratio (HR) for the effects of biomarker groups. The following chapter focuses on conducted research for the development of TILs scores as a prognostic biomarker for survival analysis in breast cancer

based solely in histological slides.

Amgad, M. et al. [49, 50]. assessed three variants of the TILs score:

1. Number of TILs / Stromal area
2. Number of TILs / Number of cells in stroma
3. Number of TILs / Total Number of cells

The results performed on the BCSS and NuCLS breast carcinoma datasets [22, 51] (the source datasets for TCGA part of TiGER dataset) showed the most prognostic TILs score to be the number of TILs divided by the total number of cells within the stromal region. A further breast cancer study [52] showed that the binarized tumor TILs infiltration fraction is predictive of survival, by analyzing the proportion of pixels in the image that were predicted as containing tumor as well as lymphocytes (number of pixels predicted as lymphocyte and tumor divided by the number of pixels predicted as tumor). Bai, et al. [53] also found associations of clinical outcomes in breast cancer with TILs scores based on the number of TILs divided by the number of TILs and tumor cells detected.

The stromal TILs (sTILs) have been shown to have prognostic value in HER2+ breast cancer and TNBC [49]. sTIL density was found significantly prognostic for OS not only while applied on H&E slides but IHC as well. [54] Applied on the TCGA-BRCA mixed with non publicly available dataset, Thagaard, J. et al. [55] tried to mimic the approach of the pathologist and therefore defined tumor-associated stroma. Tumor-associated stroma includes a margin of 250 $\mu$ m from the border of the tumor into the surrounding stroma. The sTIL density was calculated as the number of TILs within the tumor-associated stroma per mm<sup>2</sup>. The patient cohort was then stratified into two groups: high and low sTIL density by using maximally selected rank statistics for cutpoint selection. As a result sTIL density stratified the patients significantly into two distinct prognostic groups. For continuous variables, the sTIL density was divided by 300 and higher sTILs scores were associated with significantly prolonged overall survival. For the TCGA-BRCA dataset, a further TIL score was found significant as the overlapping area between lymphocyte-dense regions and stromal regions divided by the size of the stromal regions. [56] Whereas a study, that focused on TNBC cases of TCGA, did not observe any differences in OS neither while using a continuous variable of manually annotated TILs (scored by a pathologist and partitioned into eight different groups, e.g. < 1%, 10-20%, etc.) nor after applying the log-rank test [57]. On the other hand, Fassler, D. J., et al. [58] confirmed correlation of intratumoral TIL infiltration with increased OS in breast cancer in the TCGA-BRCA cohort. TIL infiltrate percentage was calculated as the number of predicted patches that were classified as positive for tumor and lymphocyte divided by total number of cancer patches. Another used definition of sTILs was the percentage of tumor stroma area containing a lymphocytic infiltrate without direct contact with tumor cells [59]. Furthermore, studies found a three-scale grading system for reporting TILs status to be applicable, instead of continuous or binary grouped TILs densities [60]. More advanced TILs-based features such as the Ball-Hall Index of spatially connected TILs regions (clusters) also showed association with survival, particularly within the BRCA dataset of TCGA [61]. Hence, there is no canonic method for the automatic determination of TILs score based on

---

*2 Related work*

---

the H&E breast cancer tissue samples but number of TILs per mm<sup>2</sup> of stromal area is used most frequently.

# 3 Methods

## 3.1 Semantic segmentation

### 3.1.1 DeepLab

One of the challenges in semantic segmentation using standard CNNs is that as the input feature map goes through the network it gets smaller and the information about objects of a smaller scale can be lost. DeepLab family introduces atrous convolutions that extract more dense features which help to preserve the object's information. Compared to standard convolutions, atrous convolutions have an additional parameter, atrous rate, which is the stride at which the input is sampled (Figure 3.1 a). The atrous convolution is used in the last few blocks on features that were extracted from the backbone network (e.g. ResNet [62]).

One of the latest models in this family, DeepLabv3 [33], applies several parallel atrous convolutions with different atrous rates (Atrous Spatial Pyramid Pooling, or ASPP, Figure 3.1 b) to effectively capture multi-scale information. Image-level features, or image pooling, are also applied to incorporate global context information. Those are calculated by applying global average pooling on the last feature map of the backbone. After applying all the operations in parallel, the results of each operation along the channel is concatenated and  $1 \times 1$  convolution is applied to get the output. The addition of atrous convolutions allows the enlargement of the field of view without increasing the size of the filtering kernel, therefore no increase in the computation time.

### DeepLabv3+

The reproduction of shape contours during semantic image segmentation remained difficult with DeepLabv3 [34]. DeepLabv3 bilinearly upsamples the logits both during training and evaluation (Fig. 3.2 a), hence the improvements were made to employ the encoder-decoder structure (Figure 3.2) to avoid using a naive decoder. DeepLabv3+ [34] adds the decoder

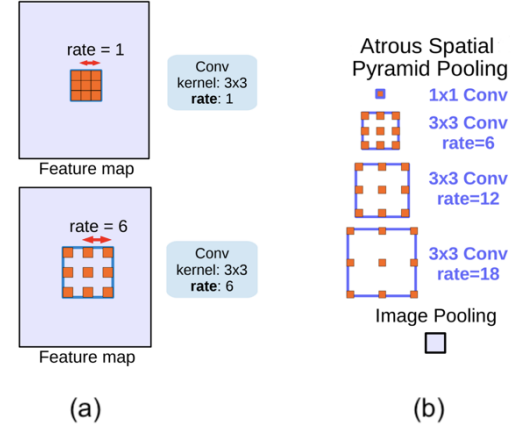


Figure 3.1: (a) Atrous convolution, (b) ASPP augmented with Image Pooling (or Image-level features) [33]

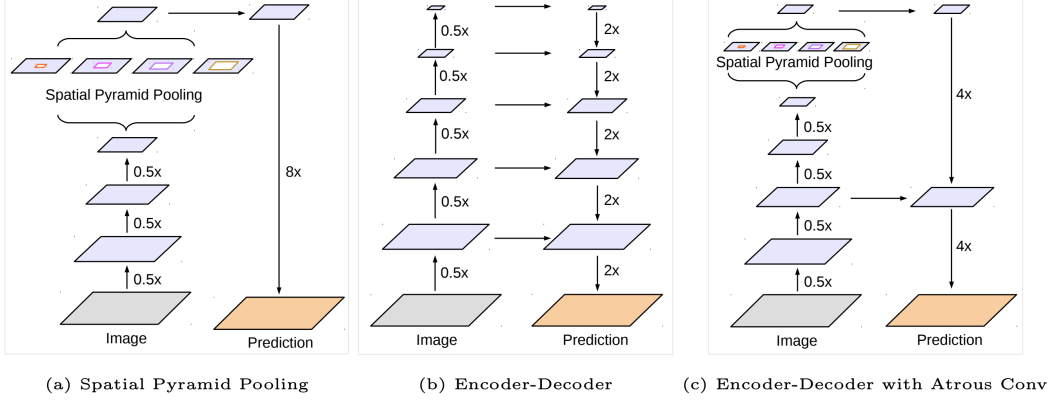


Figure 3.2: The spatial pyramid pooling module of DeepLabv3 (a), the encoder-decoder structure (b) and DeepLabv3+ adaptation (c) [34]

module on top of the encoder output, as shown in Fig. 3.3. In the decoder module, the  $1 \times 1$  convolution reduces the channels of the low-level feature map from the encoder module which is then concatenated with the DeepLabv3 feature map and the  $3 \times 3$  convolution obtains sharper segmentation results. As a result, DeepLabv3+ holds rich semantic information from the encoder module, while the detailed object boundaries are recovered by the decoder module and the spatial information is retrieved.

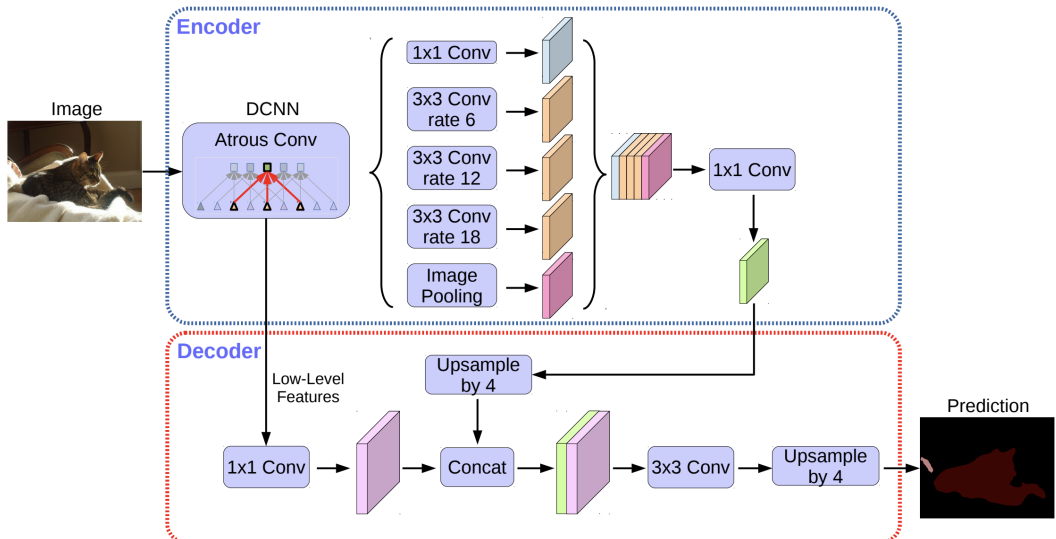


Figure 3.3: DeepLabv3+ architecture. DeepLabv3 as encoder and proposed decoder structure for semantic image segmentation. [34]

### 3.1.2 Transformers

Transformers [63] were originally designed for the neural machine translation problem in NLP to capture long-range dependencies among words in a sentence. Their architecture converts one sequence into another one based on encoder-decoder architecture, but it differs from the previously existing sequence-to-sequence models because it does not imply any Recurrent Networks.

The input and output are first embedded into an  $n$ -dimensional space. Since the network and the self-attention are permutation invariant, the positional encoding is added to create a representation of the position of the word in the sentence. The following modules consist mainly of Multi-Head Attention and Feed Forward layers. Encoder (Figure 3.4, left) and decoder (Figure 3.4, right) are composed of those modules that can be stacked on top of each other  $N \times$  times.

Self-attention is a sequence-to-sequence operation. It takes a weighted average over all the input vectors using dot product. Scaled Dot-Product Attention (Figure 3.5, left) can be described by the following equation:

$$\text{Attention}(Q, K, V) = \text{softmax}\left(\frac{QK^T}{\sqrt{d_k}}\right)V \quad (3.1)$$

where in the context of the translation problem,  $Q$  is a matrix of vector representation of one word in the sequence,  $K$  contains vector representations of all the words in the sequence and  $V$  contains again the vector representations of all the words in the sequence. For the multi-head attention modules in the encoder and decoder,  $V$  consists of the same word sequence as  $Q$ . However, for the attention module that is taken into account, the encoder and the decoder sequences,  $V$ , and  $Q$  are different.  $Q$ ,  $K$ , and  $V$  matrices are used to calculate the attention scores. These scores measure how much attention needs to be placed on words of the input sequence with respect to a word at a certain position. The scaling factor  $\sqrt{d_k}$  is applied to avoid large values that after applying softmax would lead to vanishing gradients.

While Scaled Dot-Product Attention focuses on the whole sentence, Multi-Head Attention approaches different segments of the words. The word vectors are divided into a fixed number (number of heads) of parts, and then within Multi-Head Attention (Figure 3.5, right) the attention mechanism is repeated multiple times on those separate parts with linear projections of  $Q$ ,  $K$ , and  $V$ . Since the Feed-Forward layer is expecting just one matrix, a vector for each word, the outputs are linearly concatenated. This allows the system to learn from different representations of  $Q$ ,  $K$ , and  $V$ .

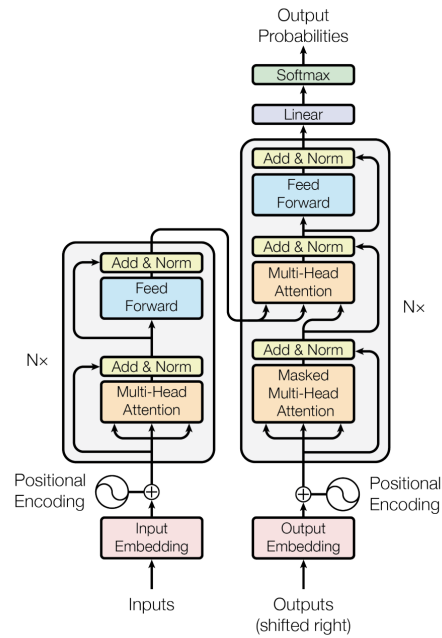


Figure 3.4: Transformer model architecture. [63]

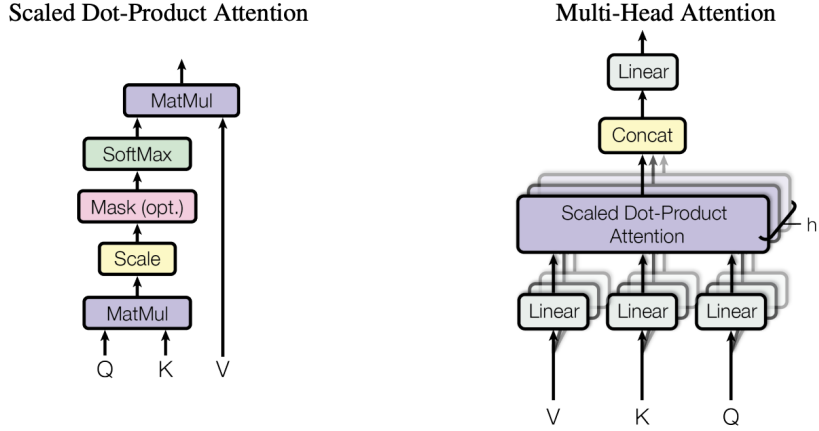


Figure 3.5: Scaled Dot-Product Attention (left). Multi-Head Attention consists of several attention layers running in parallel (right). [63]

To add element-wise non-linearity transformation of incoming vectors, the transformer includes feed-forward networks. It processes the output from one attention layer so that it fits better for the next attention layer. Each of the layers in the encoder and decoder contains a fully connected feed-forward network, which is applied to each position separately and identically. These feed-forward layers can be described as a separate, identical linear transformation of each element from the given sequence.

Naive application of the transformers approach into the image domain would require evaluation of relations between each pixel and every other pixel, which is obviously not scalable. The Visual transformer (ViT) [64] is the first work to prove that a pure Transformer can achieve state-of-the-art performance in image classification. ViT converts the input image into a 1D series by cutting it into patches and feeding it to a linear layer. It yields a patch embedding. Position embeddings are added to the image patch embeddings. Adding the learnable position embeddings to each patch allows the model to learn the structure of the image. The rest of the pipeline is a standard encoder and decoder blocks of the transformer. The decoder learns to map patch-level encodings coming from the encoder to patch-level class scores. Next, these patch-level class scores are upsampled by bilinear interpolation to pixel-level scores.

### SegFormer

SegFormer [46] is a positional-encoding-free transformer based semantic segmentation method. As depicted in Figure 3.6, it consists of two main modules: a hierarchical Transformer encoder to generate high-resolution coarse features and low-resolution fine features, and a lightweight All-MLP decoder to fuse these multi-level features and produce the final semantic segmentation mask.

The  $H \times W \times 3$  input image is forwarded to the hierarchical Transformer encoder to obtain multi-level features at  $\frac{1}{4}, \frac{1}{8}, \frac{1}{16}, \frac{1}{32}$  resolution after passing through four transformer blocks.

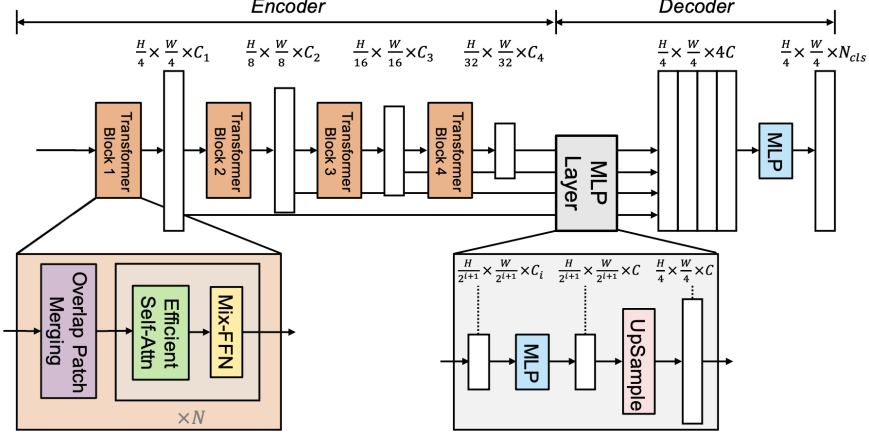


Figure 3.6: SegFormer consists of two main modules: A hierarchical Transformer encoder to extract coarse and fine features; and a lightweight All-MLP decoder to directly fuse these multi-level features and predict the semantic segmentation mask. “FFN” indicates feed-forward network. (modified image [46] according to the official implementation)

Each transformer block consists of three modules: Overlap Patch Merging, and classical transformer building blocks: Self-Attention and Feed-forward network.

The standard transformer receives input as a 1D sequence (such as word embeddings in the previous chapter 3.1.2). To handle images, those need to be reshaped into a sequence of flattened 2D patches. Overlapped Patch Merging produces features given an image and parameters: patch size  $K$ , stride between two adjacent patches  $S$ , and padding size  $P$ . In the original paper [46] those are set to  $K = 7$ ,  $S = 4$  and  $P = 3$ . Therefore the input is split into fixed-size patches, which then go through a linear projection. The result is a hierarchical feature map  $F_i$  with a resolution  $\frac{H}{2^{l+1}} \times \frac{W}{2^{l+1}} \times C_i$  where  $i \in \{1, 2, 3, 4\}$  and  $C_{i+1}$  is larger than  $C_i$ . By performing this with overlapped patches SegFormer aims to preserve the local continuity around those patches.

The main computation bottleneck of each transformer block in encoder is the self-attention layer. In SegFormer, before applying the self-attention according to the formula 3.1, the sequence  $K$  is reduced by ratio  $R$ :

$$\hat{K} = \text{Reshape}\left(\frac{N}{R}, C \cdot R\right)(K)$$

$$K = \text{Linear}(C \cdot R, C)(\hat{K})$$

where  $N = H \times W$ ,  $\text{Reshape}\left(\frac{N}{R}, C \cdot R\right)(K)$  refers to reshaping  $K$  to the shape of  $\frac{N}{R} \times (C \cdot R)$ , and  $\text{Linear}(C \cdot R, C)(\hat{K})$  refers to a linear layer taking a  $(C \cdot R)$ -dimensional tensor as input and generating a  $C$ -dimensional tensor as output. Therefore, the new  $K$  has dimensions  $\frac{N}{R} \times C$ . In original experiments,  $R$  was set to  $[64, 16, 4, 1]$  from stage-1 to stage-4 and resulted in a reduction of the complexity of the self-attention mechanism.

Mix-FFN (feed-forward network) can be formulated as:

$$x_{out} = MLP(GELU(Conv3 \times 3(MLP(x_{in})))) + x_{in}$$

where  $x_{in}$  is the feature from the self-attention module. By using  $3 \times 3$  convolution and zero padding in a feed-forward network SegFormer aims to leak pixel location information since it is a positional-encoding-free method.

The multi-level features are then passed to All-MLP decoder to predict the segmentation mask at  $\frac{H}{4} \times \frac{W}{4} \times N_{cls}$  resolution, where  $N_{cls}$  is the number of classes. The proposed All-MLP decoder consists of four main steps. First, multi-level features from the encoder go through an MLP layer to unify the channel dimension (3.2). Then, features are up-sampled to  $\frac{1}{4}$ th of the original image (3.3). Third, an MLP layer is adopted to fuse the concatenated features (3.4). Finally, another MLP layer takes the fused feature to predict the segmentation mask (3.5).

$$\hat{F}_i = MLP(C_i, C)(F_i), \forall i \quad (3.2)$$

$$\hat{F}_i = Upsample\left(\frac{H}{4} \times \frac{W}{4}\right)(\hat{F}_i), \forall i \quad (3.3)$$

$$F = MLP(4C, C)(MLP(\hat{F}_i)), \forall i \quad (3.4)$$

$$M = MLP(C, N_{cls})(F) \quad (3.5)$$

where  $F_i$  is the the feature and  $M$  is the final mask.

### 3.1.3 TILs segmentation postprocessing

As tissue segmentation, TILs detection was approached as a semantic segmentation problem with detection bounding boxes transformed into pseudo-segmentation masks (further details in Data section 4.1). TILs segmentation results were first processed with non-maximum suppression to extract local maxima, then obtain point annotation of each TIL, and compare with ground truth annotations by finding a match with the Hungarian Algorithm.

#### Non-maximum Suppression (NMS)

Non-maximum Suppression is a class of algorithms to select one entity out of many overlapping entities. In terms of detection models, used to find the best-fitting bounding box out of all predicted bounding boxes for the same object [65]. Each proposal comes with a confidence score. One by one the bounding box with the highest score is selected to keep and compared to all bounding boxes by calculating Intersection Over Union (IoU). If a comparison scores the IoU higher than some defined threshold, those bounding boxes out of the pool are eliminated. The process is repeated by picking the highest confidence bounding box out of the remaining pool of proposals until there are any.

In terms of TILs segmentation, there are no proposed bounding boxes and no scores. Nonetheless, to obtain good centroids for each TILs prediction, the segmentation posteriors need to be condensed to local maxima. The NMS application will in this case appropriately filter the segmentation posteriors with a kappa threshold and the segmentation borders refined to get a clear TIL region annotation with a suitable kernel size used for dilation.

### Hungarian algorithm

To evaluate the match of predicted TILs and ground truth annotations, it is not enough to compare the coordinates. Each TIL should be annotated with a point annotation of one pixel, it is aimed to be placed in the center but really placed in the center of a predicted TIL area, which is not perfect. The goal is to find the pairs of coordinates that indicate the same TIL object. Matching between the ground truth set and predictions can be solved as an assignment problem with the Hungarian algorithm [66]. It is a combinatorial optimization algorithm that solves the problem in polynomial time complexity. The distance matrix  $n \times m$  between all annotated ( $n$ ) versus predicted ( $m$ ) TILs is the cost matrix of each of the prediction coordinates to match any of the ground truth coordinates. The goal is to assign the ground truth coordinates to the prediction coordinates to minimize the total distance. The algorithm can be introduced as step-by-step instruction:

- Step 1: For each row, subtract the smallest element of the row from each of its elements.
- Step 2: For each column, subtract the smallest element of the column from each of its elements.
- Step 3: Cover all zeros with a minimum number of lines

In the resulting matrix cover all zeros using a minimum number of horizontal and vertical lines. If there are  $n$  lines, Step 5.

- Step 4: Find the smallest element that is not covered by a line in Step 3. Subtract it from all uncovered elements, and add it to all elements that are covered twice. Step 3.
- Step 5: Assignment pairs are indicated by the positions of the zeros in the cost matrix.

As a result, the assignment pairs include the matching of ground truth TILs coordinates to the prediction coordinates that minimize the total distance. If desired, the pairs can be filtered by minimal allowed distance. This work uses the `scipy.optimize.linear_sum_assignment` implementation of the Hungarian algorithm.

## 3.2 Survival Analysis

The overall survival (OS) is the primary endpoint for prognostic analysis in this thesis, hence time to the event (death) is of interest. Survival data are generally described and modeled in terms of two related probabilities, namely survival and hazard. [67] This thesis focuses on non-parametric models to avoid making any additional assumptions about the distributions. Throughout the analysis, the python library `lifelines` [68] was used. The survival probability

$S(t)$  is the probability that an individual survives from the time origin (in our case diagnosis of breast cancer) to a specified future time  $t$ . It can be denoted as:

$$S(t) = \Pr(T > t) = 1 - F(t) = \int_t^\infty f(x)dx = \text{Probability of surviving past time } t$$

where  $T$  is a random variable that indicates the time until the event of interest (death).  $F(t)$  and  $f(t)$  are the cumulative distribution function and probability density function of  $T$ . The hazard is the probability that an individual who is under observation at a time  $t$  has an event at that time:

$$h(t) = \lim_{\delta t \rightarrow 0} \frac{\Pr(t \leq T \leq t + \delta t | T > t)}{\delta t} = \frac{f(t)}{1 - F(t)}$$

In contrast to the survival function, which focuses on not having an event, the hazard function focuses on the event occurring. So if hazard probability describes the intensity of death [69] at the time  $t$  given that the individual has already survived past time  $t$ , then the cumulative hazard is the cumulative amount of hazard up to time  $t$ . The cumulative hazard  $H(t)$ , defined as the integral of the hazard, can be calculated using the survival probability with help of the Laplace transform:

$$H(t) = \int_0^t h(x)dx = \int_0^t \frac{f(x)}{1 - F(x)}dx = -\ln(1 - F(t)) = -\log(S(t))$$

The cumulative hazard can be interpreted as the number of events that would be expected for each individual by time  $t$  if the event was a repeatable process. [67]

### 3.2.1 Kaplan–Meier estimator

The survival probability can be estimated nonparametrically from observed survival times, both censored and uncensored, using the Kaplan–Meier method. The estimated probability of surviving past time  $t$  is calculated as:

$$\hat{S}(t) = \prod_{i:t_i \leq t} \left(1 - \frac{d_i}{n_i}\right)$$

where  $n_i$  is the number of patients alive before  $t_i$  (and not censored) and  $d_i$  is the number of observed events at  $t_i$ .  $t_0 = 0$  and  $S(0) = 1$ . The estimated probability is a step function that changes value only at the time of an event. To characterize the survival in a homogeneous group often the empirical survival function is visualized with Kaplan–Meier plot.

### 3.2.2 Cox model

Additionally to the event time, there is often access to other covariates of individuals (e.g. age, gender, BMI, etc.). Often the goal is to understand how the covariates affect the survival function of the event. [69] Let  $C$  denote those covariates. The conditional survival function can be formulated as followed:

$$S(t|c) = \Pr(T > t | C = c) = \text{Probability of surviving past time } t \text{ given } c$$

### 3 Methods

---

Hence, the conditional hazard function and conditional cumulative hazard are:

$$H(t|c) = -\log(S(t|c)), \text{ hence } h(t|c) = -\frac{\partial \log S(t|c)}{\partial t}$$

The Cox proportional hazard model models the hazard function  $h(t|C = c)$  as:

$$h(t|C = c) = h_0(t) \exp(c^T \beta)$$

where  $\beta$  is the vector of coefficients for each of the covariates and  $h_0(t)$  is the baseline hazard function. The hazard ratio, or **risk**, is the exponential of  $\beta_i$  value  $\eta_i = \exp(\beta_i)$  and the baseline hazard describes how the risk of event per time unit changes over time at baseline levels of covariates. The Cox model assumes that the covariates have a linear multiplication effect on the hazard function and the effect stays the same over time.

$$\frac{h(t|c_i)}{h(t|c_j)} = \frac{h_0(t) \exp(c_i^T \beta)}{h_0(t) \exp(c_j^T \beta)} = \frac{\exp(c_i^T \beta)}{\exp(c_j^T \beta)} = \exp((c_i - c_j)^T \beta)$$

The ratio of the hazard function between two individuals with different covariates  $c_i$  and  $c_j$  is a constant over time since  $h_0(t)$  was canceled out. Hence the name, proportional hazard model. The conditional hazard function is:

$$H(t|c) = \exp(c^T \beta) \int_0^t h_0(s) ds = \exp(c^T \beta) H_0(t)$$

It yields a conditional survival function:

$$S(t|c) = \exp(-H(t|c)) = \exp(-\exp(c^T \beta) H_0(t)) = \exp(-H_0(t))^{\exp(c^T \beta)} = S_0(t)^{\exp(c^T \beta)}$$

Estimation of the parameter  $\beta$  is often done by maximizing the partial likelihood function  $\hat{\beta}_n = \text{argmax}_{\beta} \hat{L}_n(\beta)$ , where:

$$\hat{L}(\beta) = \prod_{i=1}^n \frac{h(T_i|C_i)}{\sum_{j:T_j \geq T_i} h(T_j|C_j)} = \prod_{i=1}^n \frac{\exp(C_i^T \beta)}{\sum_{j:T_j \geq T_i} \exp(C_j^T \beta)}$$

A positive sign of  $\beta_i$  indicates a higher risk of an event, hence the probability for the event for that particular subject is higher. Likewise for a negative signed  $\beta_i$ , lower risk, and lower probability. The actual value of  $\beta_i$  plays a role as well. Values less than one will reduce the hazard and values greater than one, increase it.

A model's accuracy can be quantified based on concordance. [70] It is a measure of the rank correlation between predicted risks and observed time points. It is defined as the ratio of correctly ordered (concordant) patient pairs to all concordant and discordant patient pairs. Let  $i, j$  be a patient pair. If a model predicts a higher risk for the first patient ( $\eta_i > \eta_j$ ), for it to be a concordant pair first patient should have a shorter survival time in comparison with the other patient ( $T_i < T_j$ ) and similarly if lower risk then longer survival time,  $\eta_i < \eta_j$  &  $T_i > T_j$ . If both patients are censored the pair is discarded. If only one patient is censored, the pair is not discarded only if the other patient experienced the event before the censoring time. By

### 3 Methods

---

construction, concordance must be between 0 and 1, with 1 representing the perfect agreement between model and observation and 0.5 representing random guesses.

Additionally, to estimate the goodness-of-fit the p-value is determined. The Wald test is typically used to evaluate the significance of a variable in the model estimated with the maximum likelihood function. The null hypothesis is that the model does not fit the data well. The Wald statistic tests, whether  $\beta_i$  coefficient is statistically significantly different from 0 and is defined as:

$$W = \frac{(\hat{\beta}_n - \beta_0)^2}{var(\hat{\beta}_n)}$$

If the true coefficient was  $\beta_0$ , then the sampling distribution of the Wald test statistic should be approximate  $\mathcal{N}(0,1)$ . The p-value gives the probability of observing a test statistic as extreme as the one observed if the sampling distribution was  $\mathcal{N}(0,1)$ . If the p-value is small, the observed test statistic is very unlikely under the null hypothesis. And the significance level of 0.05 indicates that there is a 5% risk of being wrong by concluding that the model fits the data well when it doesn't.

## 4 Data

To give an overview of the data used as well as extend the scheme presented in the Introduction chapter (Figure 1.1), refer to Figure 4.1. The following sections provide more details about the data.

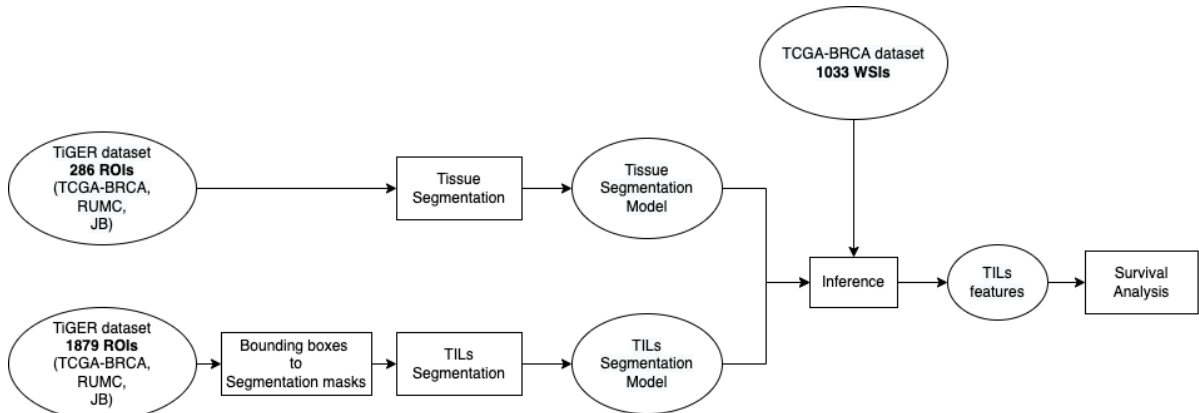


Figure 4.1: Scheme of tasks completed in this thesis accomplitmented with the data sources and counts.

### 4.1 Segmentation

The data for tissue and TILs segmentation originates from publicly available Tumor InfiltratinG lymphocytes in breast cancER (TiGER) challenge dataset containing digital pathology images of Her2 positive (Her2+) and Triple Negative (TNBC) breast cancer whole-slide images (WSIs), regions of interest (ROIs), and manual annotations. More specifically, the WSIROIS dataset was used for model training, validation, and testing (see Table 4.1). It includes 195 WSIs of breast cancer core-needle biopsies and surgical resections with pre-selected ROIs and manual annotations. TiGER data, both at WSI and ROI level, was released at a spacing (pixel size) of approximately  $0.5 \mu\text{m}/\text{px}$  (at  $20\times$  magnification ), more information is available on the original challenge website<sup>1</sup>. The TiGER tissue annotations include eight labels that were reduced to three (see Table 4.2). The training masks were generated using available XML files. In the provided mask images, in certain cases, regions not included in ROIs and non-annotated regions in ROIs were marked with the same label, which could not be directly used for training (see Ground truth in Figure 5.5).

<sup>1</sup><https://tiger.grand-challenge.org/Data/>

Source	Tissue			TILs		
	slides	ROIs	median ROI size #pixels [k]	slides	ROIs	median ROI size #pixels [k]
TCGA-BRCA	151	151	4 983	124	1744	20
RUMC	26	81	1 312	26	81	1 312
JB	18	54	1 465	18	54	1 465
	195	286		168	1879	

Table 4.1: TiGER data overview. Sources: Cancer Genome Atlas Breast Invasive Carcinoma (TCGA-BRCA), Radboud University Medical Center (RUMC) and Jules Bordet Institute (JB). Tissue slides and ROIs refer to the segmentation images and annotations whereas TILs prefix specifies the data for TILs detection provided by the challenge.

TiGER Tissue Label	Share	ID	new ID	new Tissue Label
Invasive tumor	0.283	1	1	Tumor
In-situ tumor	0.029	3	1	Tumor
Tumor-associated stroma	0.286	2	2	Stroma
Inflamed stroma	0.096	6	2	Stroma
Necrosis not in-situ	0.048	5	0	Rest
Healthy glands	0.0008	4	0	Rest
Background	0.231	0	0	Rest
Rest	0.026	7	0	Rest

Table 4.2: Reduction of labels provided in TiGER challenge dataset. Resulting labels include three classes: Tumor (1), Stroma (2) and Rest (0) with shares of 0.312, 0.382 and 0.306. Shares were calculated by dividing the number of pixels belonging to some label by the number of the pixel in the current image and averaged over all images.

While for tissue segmentation the images and their masks could be used as directly extracted from the dataset, the data for TILs segmentation required some preprocessing. The TiGER fixed-size bounding box annotation for lymphocytes and plasma cells (see Table 4.3) was adapted for segmentation by transforming each bounding box into an annotation of the center pixel with a dilatation of three.

For the inferences the breast cancer TCGA-BRCA dataset was used, generated by the TCGA Research Network: <https://www.cancer.gov/tcga>. While there are a large number of images available in The Cancer Genome Atlas (TCGA), only the diagnostic slide were downloaded (Formalin-Fixed Paraffin-Embedded (FFPE) slides). FFPE slides are the gold standard in diagnostic medicine [71]. They are prepared by fixing a specimen in formaldehyde and then placing it in a paraffin block to section it. After generating a manifest file on TCGA dataset website ([72] for more information), which includes 1133 diagnostic slides of BRCA breast cancer patients, the files were downloaded with the GDC Data Transfer Tool (gdc-client with `--manifest` option).

---

Source	#slides	#ROIs	#cells	Number of cells per ROI		
				min	max	median
TCGA-BRCA	124	1 744	19 115	0 (44.3%)	206	1
RUMC	26	81	4 728	0 (7.4%)	657	19
JB	18	54	5 523	0 (7.4%)	608	51.5
	168	1 879	29 366			

Table 4.3: Data overview for TILs detection. Sources: Cancer Genome Atlas Breast Invasive Carcinoma (TCGA-BRCA), Radboud University Medical Center (RUMC) and Jules Bordet Institute (JB). Number of cells here refers to the number of bounding boxes that were assigned for lymphocytes and plasma cells, further named TILs.

## 4.2 Survival Analysis

TiGER challenge aims to assess the prognostic significance of computer-generated TILs scores for predicting survival by applying the Cox proportional hazards model. The survival analysis is done using a large independent test dataset that includes cases from both clinical routine and from a phase 3 clinical trial, which is not directly accessible by participants. The survival analysis within this thesis is done exclusively on publicly available TCGA-BRCA data. Where death (`vital_status = 1`) is considered as an event, and the time until the event or censoring is taken either from `days_to_death` (number of days to death from the first diagnosis) or `days_to_followup` (number of days to last follow-up from first diagnosis).

<code>vital_status</code>	#cases	median age at diagnosis [years]	median time to event [months]
Dead	146	62	37.8
Alive	919	58	26.3
	1065	58	28.7

Table 4.4: Survival data overview.

# 5 Results & Discussion

## 5.1 Tissue Segmentation

Three models were trained to segment the RGB input of H&E stained image at  $20\times$  magnification (resolution of 0.5 micron-per-pixel) into three prediction maps: tumor, stroma, and rest (not white space, but tissue that is neither tumor nor stroma, for details refer to Table 4.2). The data was separated on the patient level (or slide level, since there is one slide per patient present) into training, validation, and test with 80%, 10%, and 10% accordingly. In order to keep the distribution of the resulting patch numbers (see Table 5.2) and dataset sources fair, the patient separation in Table 5.1 was introduced.

	Train	Validation	Test
TCGA-BRCA	120	16	15
RUMC	20	3	3
JB	16	1	1
	156	20	19

Table 5.1: Split of patients across different medical sources into train, validation, and test sets for segmentation tasks.

The patches were created using a sliding window approach with  $256\times 256$  sized patches and stride equals 128. The additional rotation augmentation was applied, by rotating each patch 5 times at 9 degrees each.

	slides	ROIs	patches	Number of patches that include					
				Tumor	Stroma	Rest	1 class	2 classes	3 classes
Train	156	228	220 567	154 734 (70%)	172 046 (78%)	107 506 (49%)	63 919 (29%)	99 577 (45%)	57 071 (26%)
Validation	20	25	29 465	16 884 (57%)	22 187 (75%)	13 954 (47%)	11 171 (38%)	13 028 (44%)	5 266 (18%)
Test	19	33	30 248	18 194 (60%)	25 630 (85%)	14 787 (49%)	8 548 (28%)	15 037 (50%)	6 663 (22%)
	195	286	280 280						

Table 5.2: Overview of patches that were split into train, validation, and test sets for tissue segmentation. The percentages indicate the fraction of a specific conditioned group of patches to the number of all patches in the "patches" column.

The models were trained with the mmsegmentation toolbox [73]. All models were trained for 160K iterations with Cross Entropy Loss and standard data augmentation techniques including resizing at a random sample scale in the range of (0.5, 2.0), cropping with the maximum 0.75 of a single category present, flipping with 0.5 probability, and application of photometric distortion which includes 0.5 probability for each of the following transformations: random brightness, contrast, saturation, hue and color adjustments. The DeepLabv3+ model was taken as a baseline and trained with ResNet50 backbone, Adam optimizer, learning rate equals 0.0001 and batch size of 64. Whereas the transformer-based SegFormer-B5 (further referred to as SegFormer) architecture was trained once with the same setup of Adam optimizer, 0.0001 learning rate and batch size of 64, and additionally, as in original paper [46], using AdamW optimizer, the learning rate set to an initial value of 0.00006 and then used a poly learning rate schedule with factor 1.0 by default.

Model	FLOPs	Params	Iterations	Runtime	mDice			
					Overall	Tumor	Stroma	Rest
DeepLabv3+	44.16	43.58 M	160 K	1d 12h 2m	<b>85.25</b>	85.13	88.07	83.66
SegFormer	12.96	81.97 M	160 K	3d 4h 30m	83.44	83.83	86.32	80.16
SegFormer, AdamW	12.96	81.97 M	160 K	3d 4h 25m	84.93	85.40	87.40	82.00

Table 5.3: Overview of the trained tissue segmentation models. The runtime is given for a training on one GPU NVIDIA A100 SXM4.

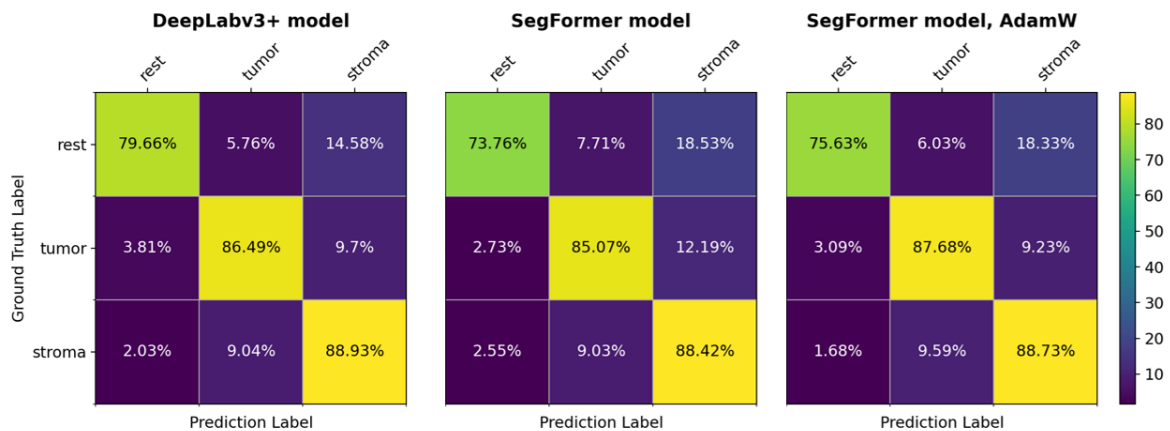


Figure 5.1: Confusion matrices on pixel level for DeepLabv3+, SegFormer and SegFormer with AdamW optimizer based on test set of 32 ROIs.

During a close investigation of test data, one slide (with the prefix TCGA-OL-A5RW-01Z-00-DX1) was excluded from the test set due to an obvious image-mask mismatch. The overall performance of the models, the number of parameters, and the resulting dice score after testing on 32 test images can be found in Table 5.3. The first thing that catches the eye is the severe

## 5 Results & Discussion

---

runtime difference of SegFormer-based methods compared to the DeepLabv3+ accompanied by doubled number of parameters. None of the SegFormer approaches outperform the DeepLabv3+, but the performance is comparable, which can be also observed in the confusion matrices in Figure 5.1. Both SegFormer-based methods show difficulty correctly segmenting rest regions, whereas SegFormer AdamW slightly outperforms DeepLabv3+ in the number of true positive detected tumor pixels.

As previously mentioned, the dataset originates from three medical institutions which make it reasonable to characterize the performance separately. The boxplots in Figure 5.2 indicate that the performance of the DeepLabv3+ and SegFormer AdamW models in TCGA-BRCA and JB groups are fairly invariant. Whereas the RUMC group accounts not only for the lower performance of SegFormer-based methods in segmenting rest regions but also for an improvement of tumor region segmentation by SegFormer AdamW model both observed in Figure 5.1.

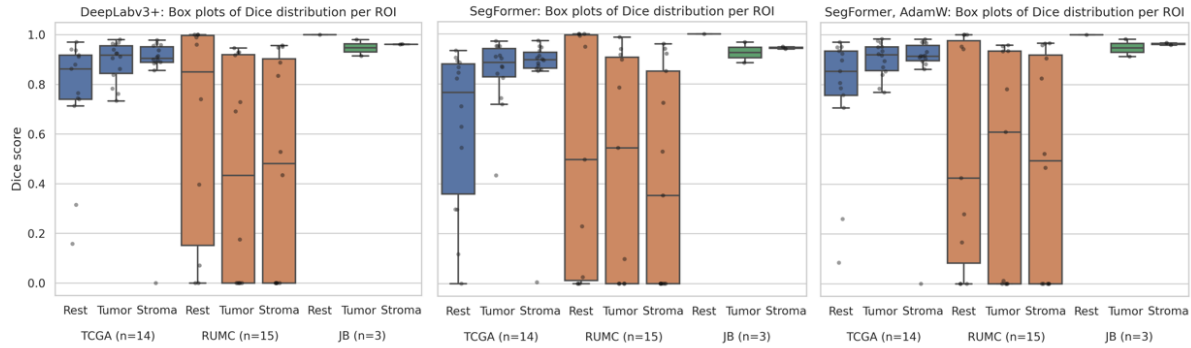


Figure 5.2: Boxplots of pixel wise calculated dice score across three datastes (TCGA-BRCA, RUMC, JB) and three segmentation labels.

The additional specialty that Figure 5.2 brings to light is the considerable number of RUMC ROIs that have been evaluated with dice scores close to zero across all models. Due to the nature of the Dice score, those can be originated from significant numbers of either false positives, false negatives, or both. According to the boxplots of precision and recall in Figure 5.4 the precision across all models has more close zero values that indicate more frequent false positives. There are clear examples, such as Figure 5.3, where the ground truth includes exclusively rest but all trained models provide multiple class predictitons. Even though there are also opposite examples of regions that were solely annotated as rest and predicted as such (which then lead to occasional dice, precision, and recall equal to one), the issue of false positives, in this case, might be solved only by finding a better dataset split.

A close look at the prediction also revealed that at some cases dice scores might suffer due to some inaccuracies in the annotations. Figure 5.5 showcases that all models were penalized for detecting a rest region inside of the tumor, which was probably learned with some dependency to the presence of white space, which also present in the same slide (the bubbles in the lower part of the image) and was annotated as rest.

## 5 Results & Discussion

---

Nonetheless, there are positive segmentation results present, such as JB ROIs depicted in Figure 5.6 and 5.7 where the performance of SegFormer AdamW is either very close or slightly better than DeepLabv3+. Curiously, in Figure 5.7 the SegFormer AdamW performs slightly better partly because this model, in contrast to the rest, did not attempt to annotate the small possibly tumorous region in the upper left corner (around (250, 200), which is not annotated in ground truth but visually highly similar to the tumor regions in this example). To decide whether this is an encouraging behavior the pathologist must be consulted, but in some cases, SegFormer AdamW manages to considerably outperform DeepLabv3+, as visualized in Figure 5.8. Yet while the SegFormer AdamW model remains promising, due to overall better performance and runtime, this thesis will use the DeepLabv3+ model for further inferences and analysis.

For model inference, the model with the best pixel-wise Dice score on the validation set was used. Patches of size  $256 \times 256$  were extracted from the tissue region at  $20\times$  magnification with a stride of 184 (for faster runtime). The whitespace was extracted by using thresholding and inference of non-background pixels was then performed.

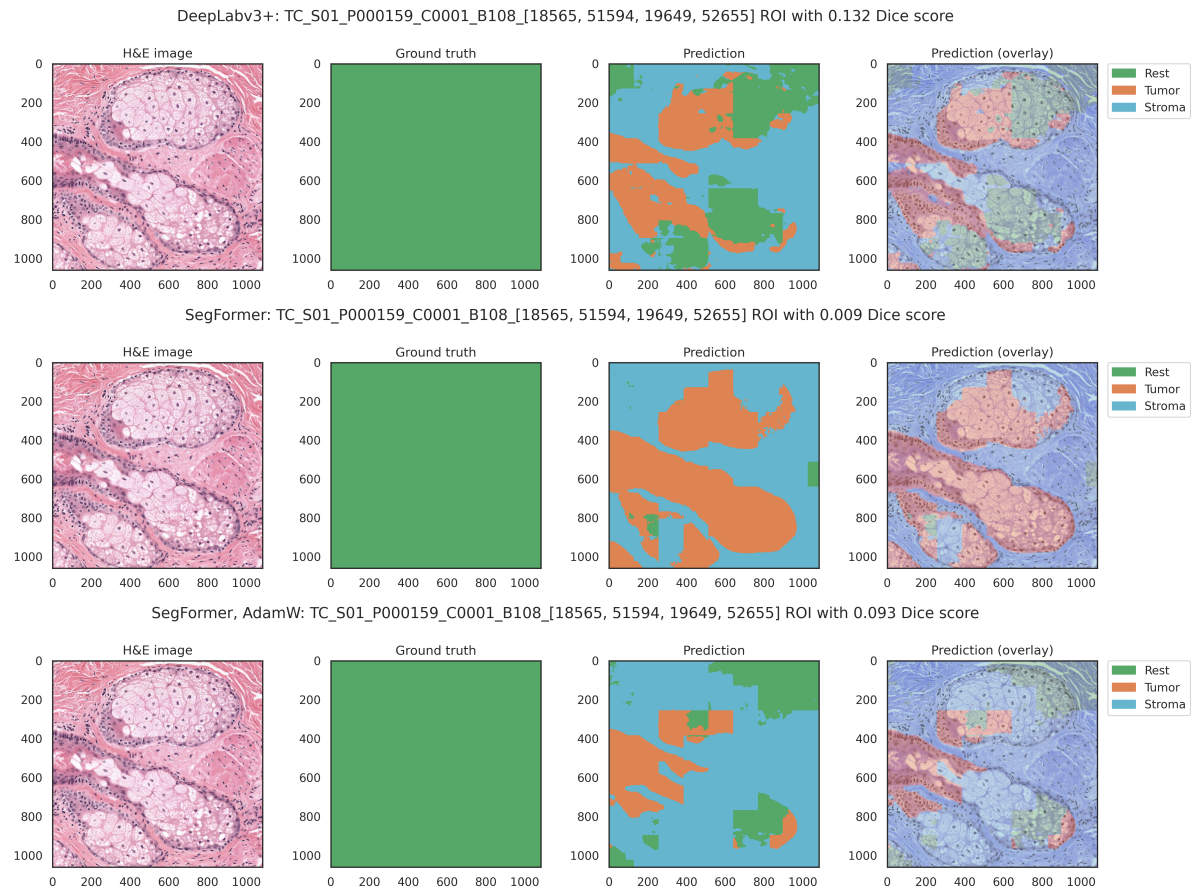


Figure 5.3: Example of rich false positive segmentation RUMC ROI that contributes to the cases of close zero dice scores.

## 5 Results & Discussion

---

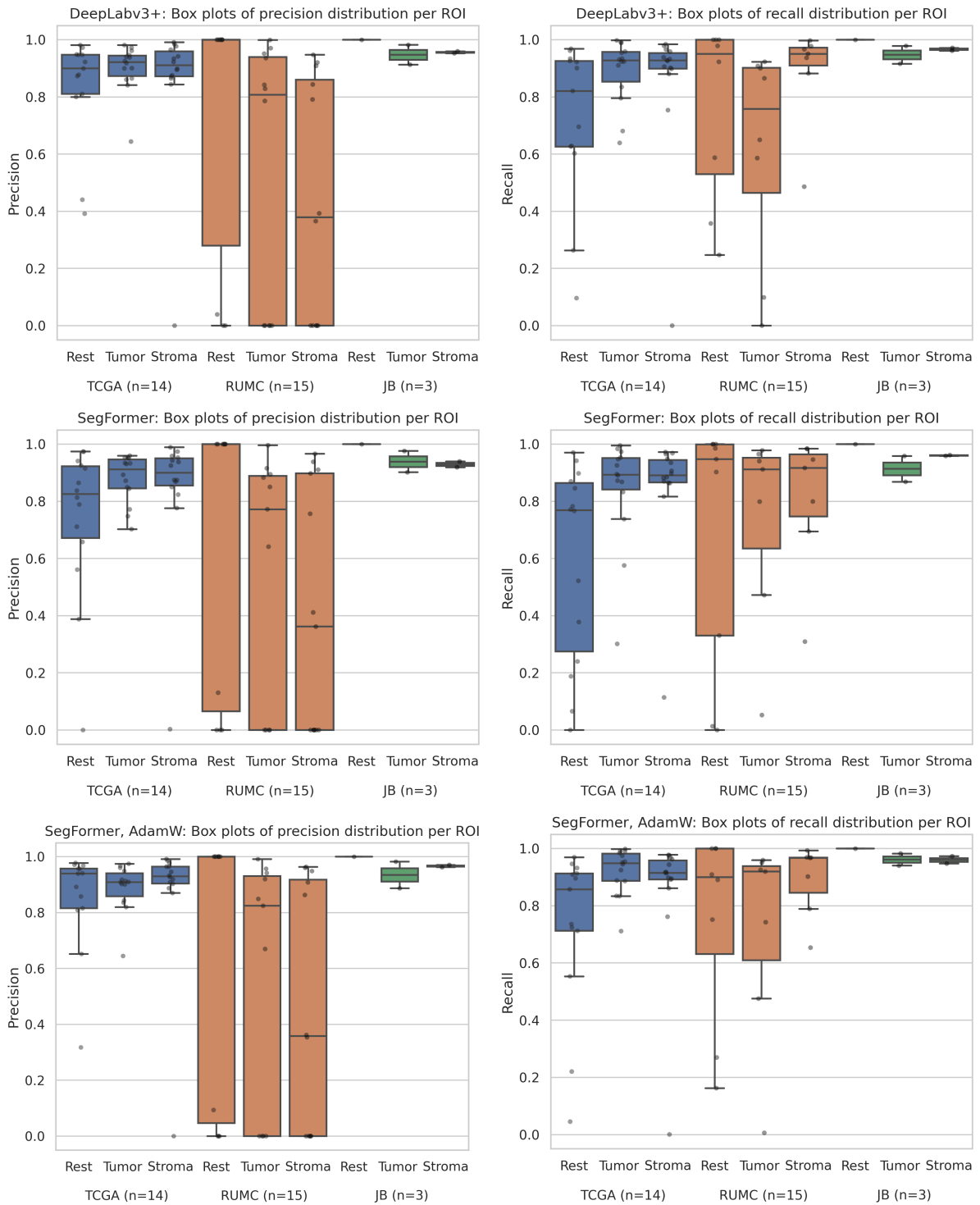


Figure 5.4: Boxplots of pixel wise calculated precision and recall across three datasets (TCGA-BRCA, RUMC, JB) and three segmentation labels.

## 5 Results & Discussion

---

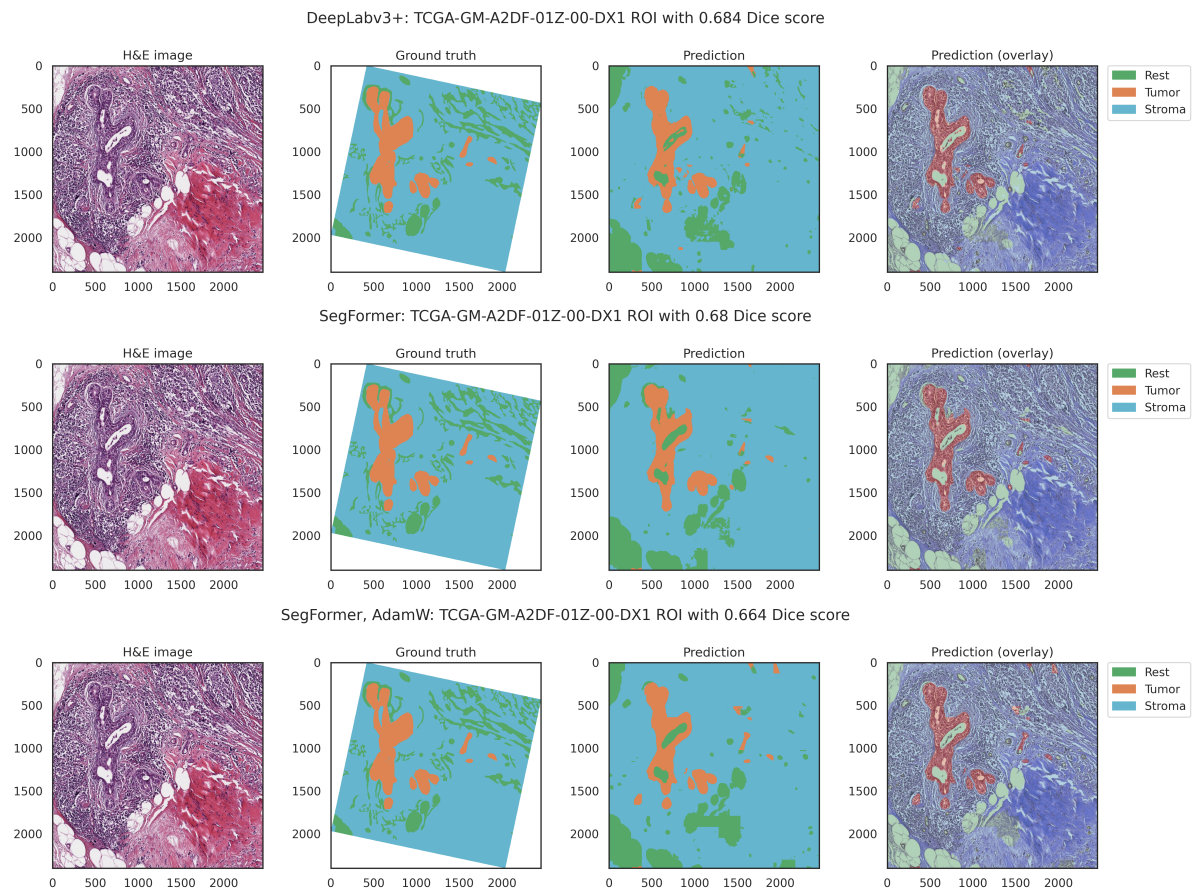


Figure 5.5: Example of a slightly devalued dice score due to some annotation inaccuracies.

## 5 Results & Discussion

---

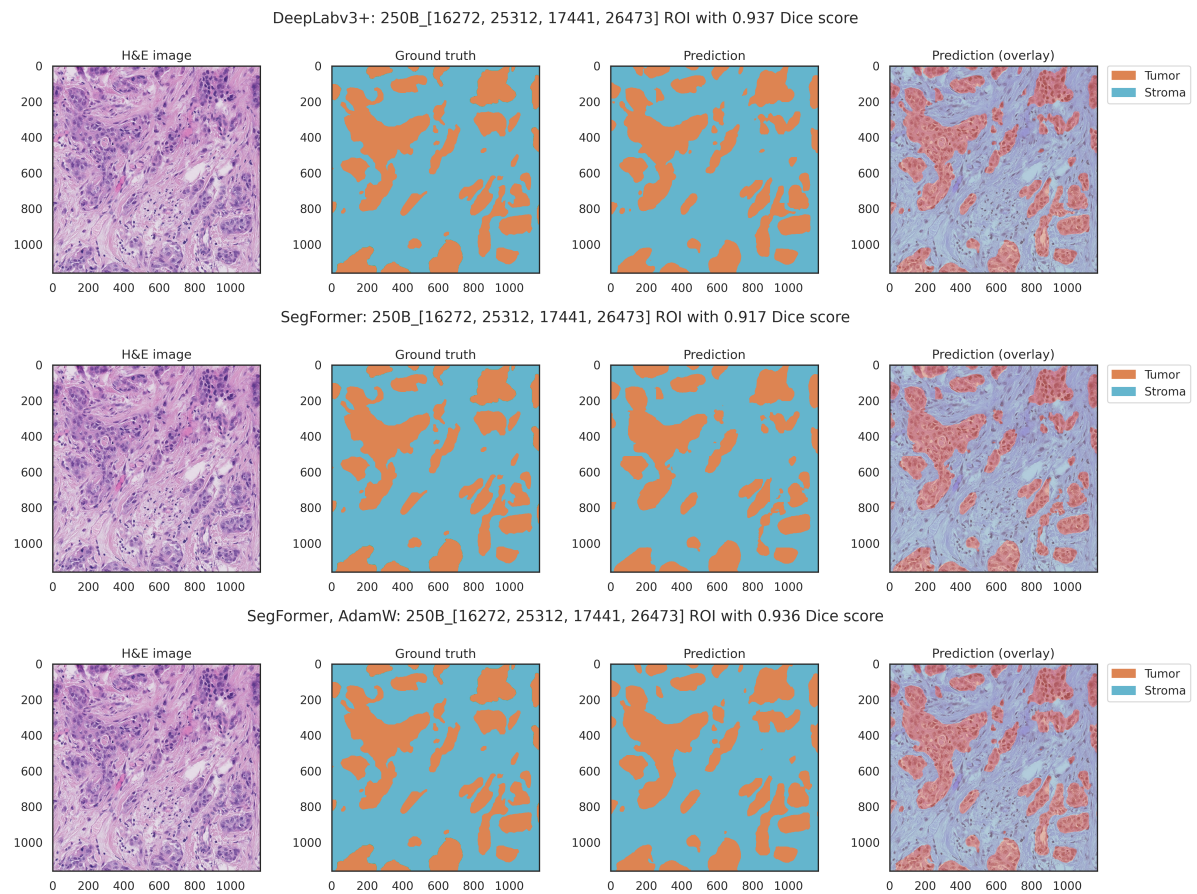


Figure 5.6: JB S\_250B ROI segmentation result.

## 5 Results & Discussion

---

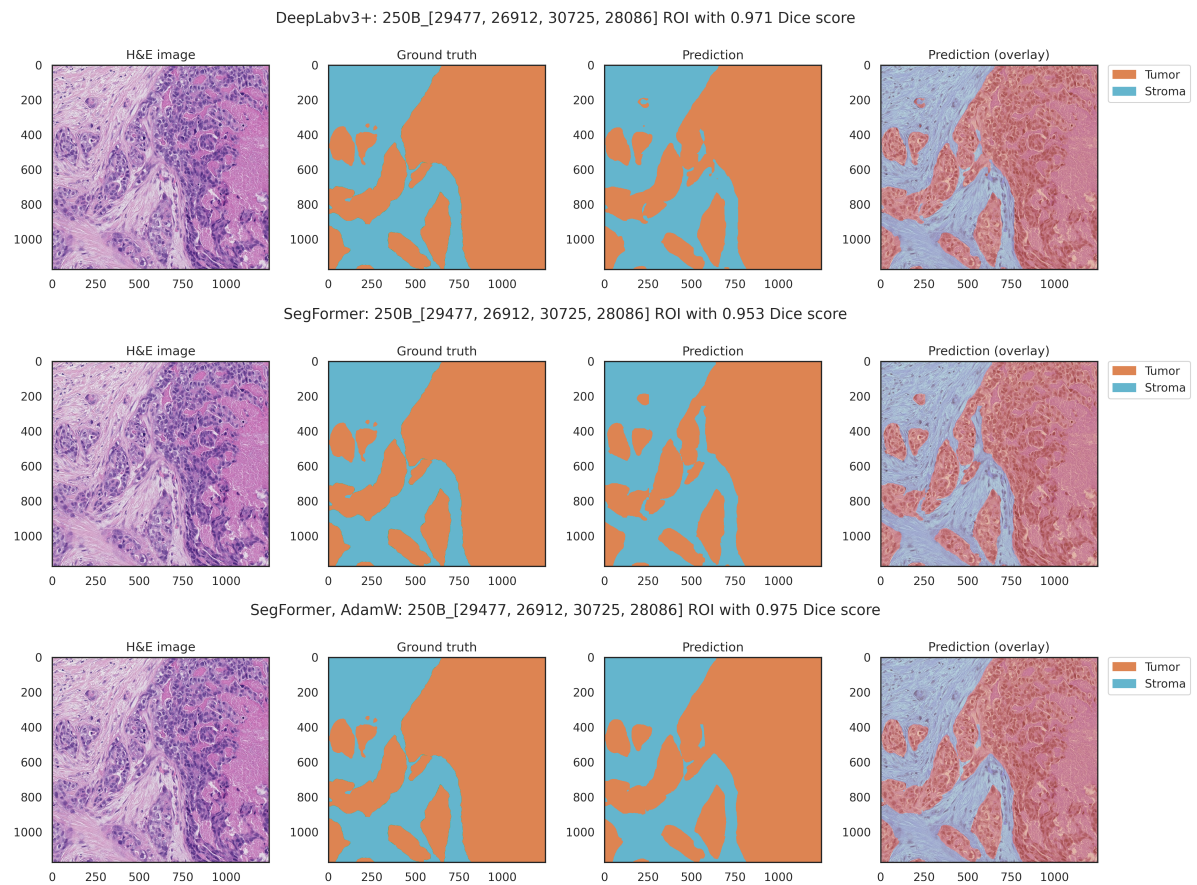


Figure 5.7: JB S\_250B ROI segmentation result.

## 5 Results & Discussion

---

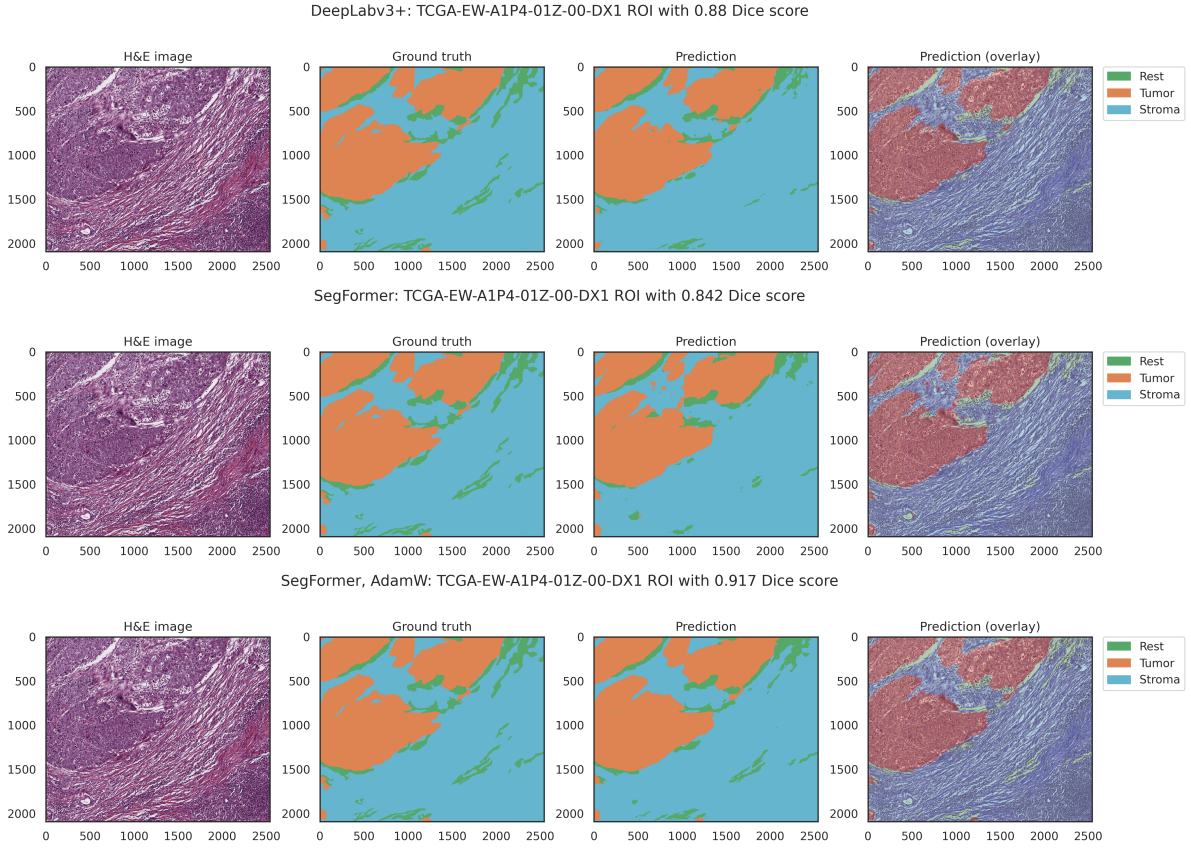


Figure 5.8: TCGA-EW-A1P4-01Z-00-DX1 ROI segmentation result.

## 5.2 TILs Segmentation

TILs segmentation task aimed to segment the RGB input of H&E stained image at  $20\times$  magnification (resolution of 0.5 micron-per-pixel) into two prediction maps: TILs and rest. The split of the patients was used similarly to the previously described in Tabel 5.1. Even though the same patients are present in this data set, the annotations originate from a different study which results in a different ROI and patch statistics shown in Table 5.4. The patches were created using a sliding window approach with  $128\times 128$  sized patches and stride equals 100. The ROIs that were smaller than  $128\times 128$  were padded. The additional rotation augmentation was applied, by rotating each patch 5 times at 9 degrees each. The column "Number of patches that include rest" in Table 5.4 seems excessive, but was still added for better data comprehension: the ROIs for TILs segmentation are either completely annotated as rest or include occasional TILs masks.

The model architectures and their parameters were used as described in 5.1: DeepLabv3+, SegFormer with Adam optimizer, and SegFormer with AdamW. An important change is an increased batch size of 128, which was allowed due to smaller patch sizes of  $128\times 128$ . In the model overview in Table 5.5 the number of parameters and iterations remain the same.

	slides	ROIs	patches	Number of patches that include			
				TILs	Rest	1 class	2 classes
Train	156	1 552	106 974	35 433 (33%)	106 974 (100%)	71 541 (67%)	35 433 (33%)
Validation	20	154	15 518	14 164 (27%)	15 518 (100%)	5 638 (60%)	3 734 (40%)
Test	19	173	9 372	3 734 (40%)	9 372 (100%)	11 354 (73%)	4 164 (27%)
	195	1 879	131 864				

Table 5.4: Overview of patches that were split into train, validation, and test sets for TILs segmentation. The percentages indicate the fraction of a specific conditioned group of patches to the number of all patches in the "patches" column.

FLOPs values are dependent on input shape, therefore it was expected to drop since the input is smaller. It is also noticed that for TILs segmentation the runtime between all three models becomes comparable in contrast to tissue segmentation (Table 5.3).

Model	FLOPs	Params	Iterations	Runtime	F1 score	Precision	Recall
DeepLabv3+	11.04	43.58 M	160 K	2d 8h 36m	0.49	0.58	0.43
SegFormer	3.24	81.97 M	160 K	2d 11h 36m	0.62	0.62	0.33
SegFormer, AdamW	3.24	81.97 M	160 K	2d 15h 19m	<b>0.66</b>	0.64	0.69

Table 5.5: Overview of the trained TILs segmentation models. The runtime is given for a training on one GPU NVIDIA A100 SXM4.

For proper evaluation the predicted TILs segmentation needed to be reduced to TILs centers (one pixel) that can be then further matched to ground truth. To get optimal centers of predicted TILs, non-maximum suppression was applied on posterior images that were clipped between 0 and 255. The search for the best-fitted parameter of kappa (threshold) and kernel size was completed on the validation set. As pictured in Figure 5.9 there were multiple experiments performed with kernel sizes in [1, 3, 5, 7, 9, 11, 13] and multiple kappas. The highest value of kappa was the median value over all posteriors. The consecutive values were the two power fractions of the median. Figure 5.9 includes two images for DeepLabv3+ (first in the first row and first in the second row) to provide a zoomed look of the tighter range. As a result, the best parameters on the validation set were chosen as kappa=21, kernel size=9 for DeepLabv3+ and kappa=64, kernel size=5 for SegFormer-based methods. The resulting centers were matched to the ground truth by applying the Hungarian algorithm that found the best assignment to match ground truth TILs with predicted ones. The allowed maximum distance for a match of predicted with ground truth TILs was set to 5  $\mu\text{m}$ .

The final results represented in Table 5.5 show that SegFormer model with AdamW optimizer strongly outperforms DeepLabv3+ and simple SegFormer. Furthermore, while

## 5 Results & Discussion

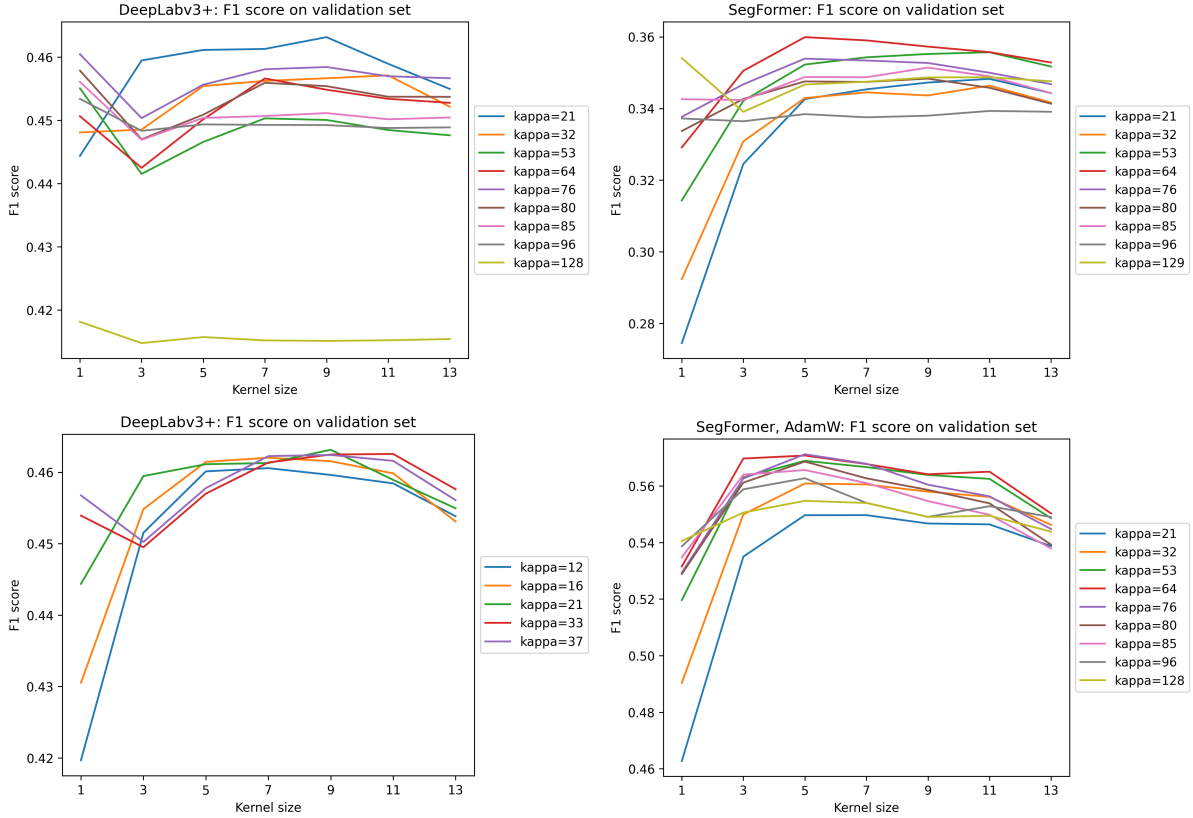


Figure 5.9: Determination process for best kappa and kernel size for DeepLabv3+ (first in the first row and first in the second row), SegFormer (second in the first row), and SegFormer with AdamW (second in the second row).

distinguishing the F1 scores between ROIs originating from different medical centers in Figure 5.10, SegFormer AdamW results show significantly better results in all subgroups.

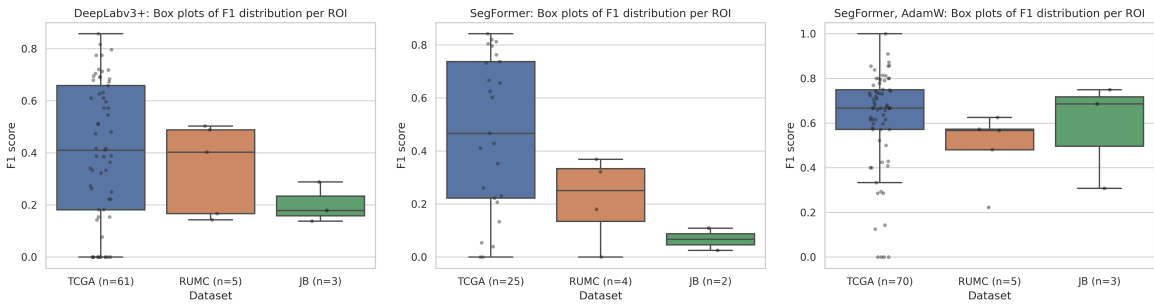


Figure 5.10: Boxplots of dice score across three datasets (TCGA-BRCA, RUMC, JB) with maximum allowed distance between ground truth and prediction equals 10 pixels (5  $\mu\text{m}$ ).

Interestingly the precision boxplots in Figure 5.11 do not show such an unequivocal superiority, where in the JB subgroup simple SegFormer manages to predict fewer false positives and ( $n=2$ ) indicates that the model managed to predict empty ROI as a complete rest region, which is not the case for any other model. In more detailed Figure 5.12 one can see the intermediate steps of how the posteriors are simplified into point segmentations and later the misted, falsely annotated and correct TILs can be compared. Even on the level of posteriors (overlaid with H&E image), it is visible that SegFormer AdamW manages to detect more regions, especially closer to the border of the image. The grids in Figure 5.12 were added for readers' convenience and are not artifacts. Taking into account all discussions above and the overall better performance, the SegFormer AdamW was considered the best model, and the model with the highest pixel-wise dice score on the validation set was taken to the next step.

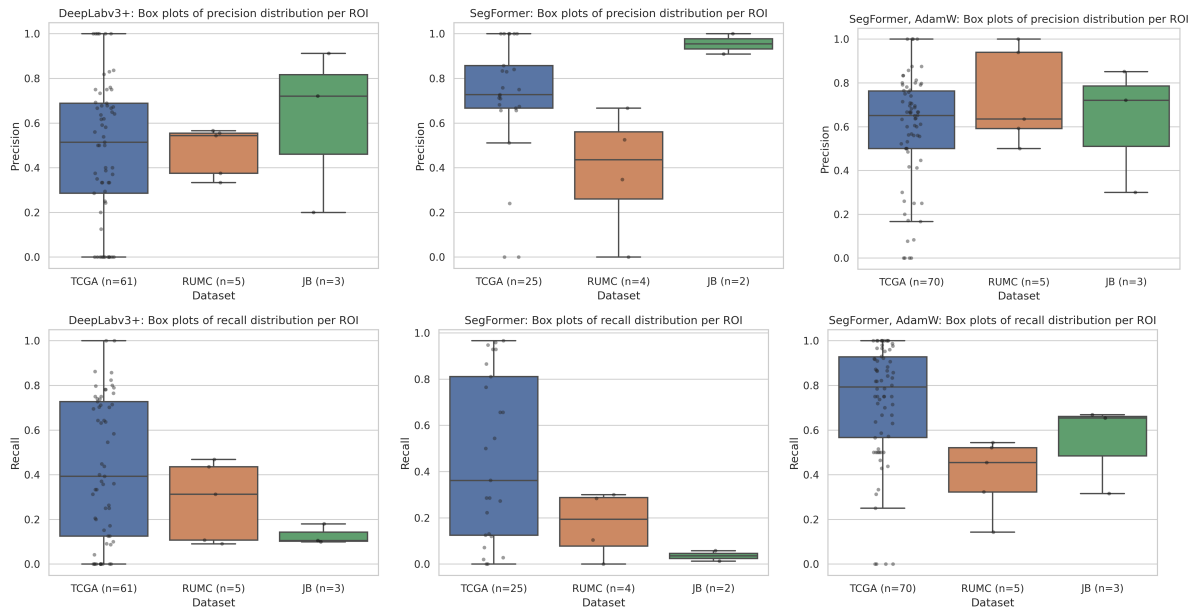


Figure 5.11: Boxplots of precision and recall across three datasets (TCGA-BRCA, RUMC, JB) with maximum allowed distance between ground truth and prediction equals 10 pixels (5  $\mu\text{m}$ ).

For model inference, the model with the best pixel-wise Dice score on the validation set was used. Patches of size  $128 \times 128$  were extracted from the tissue region at  $20\times$  magnification with a stride of 100. The whitespace was extracted by using thresholding and inference of non-background pixels was then performed.

## 5 Results & Discussion

---

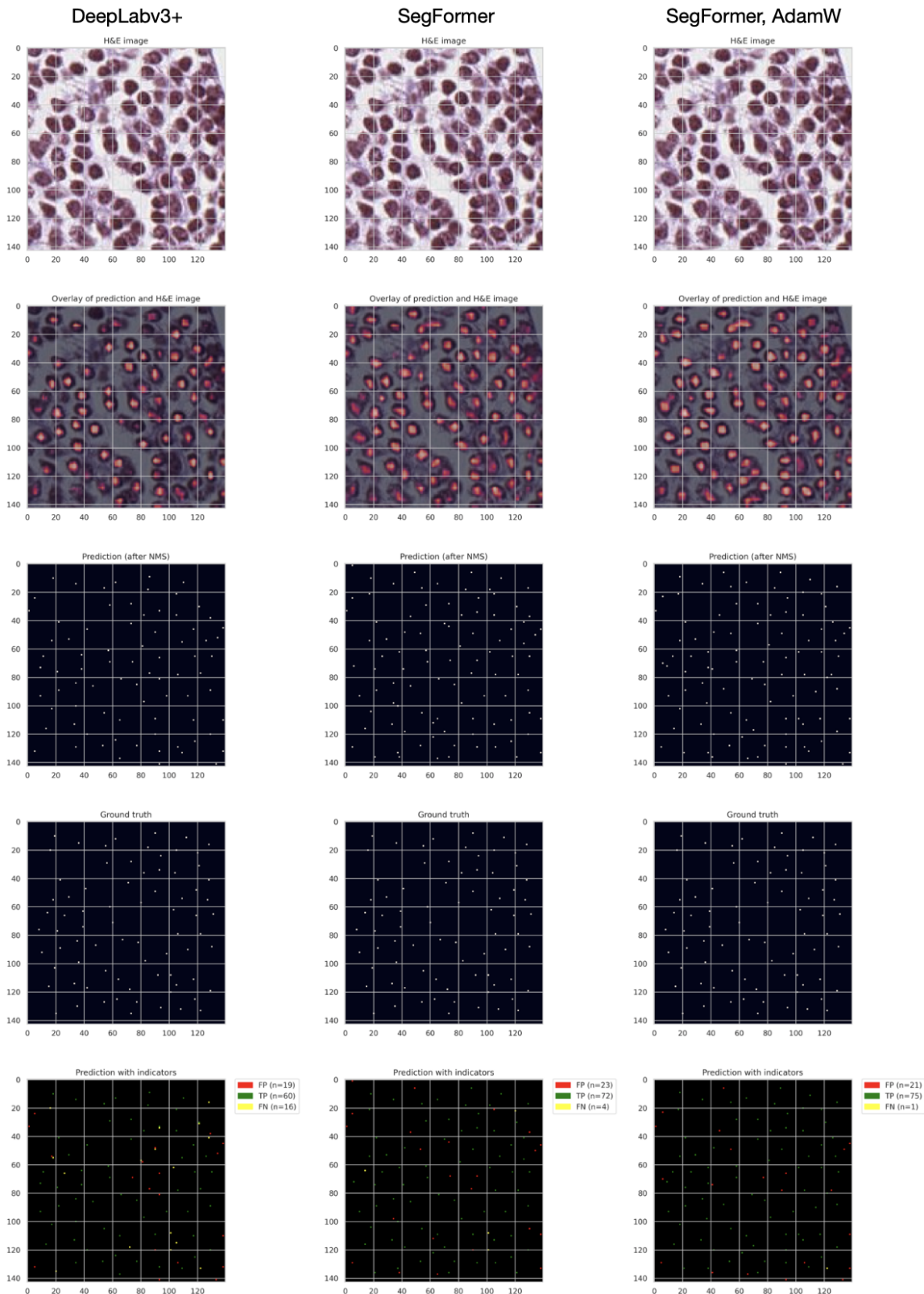


Figure 5.12: TCGA-D8-A142-01Z-00-DX12 TILs prediction with DeepLabv3+, SegFormer and SegFormer, AdamW. With 0.774, 0.842 and 0.872 F1 scores accordingly.

### 5.3 Survival Analysis

The following results are generated with DeepLabv3+ TILs detection. Missing heterogeneity features. Waiting for the results to generate. If everything goes wrong, those are the final results. Hopefully not.

The patients from TCGA-BRCA clinical data with negative or not complete event times were removed. The remaining 1005 patients were used for survival analysis. 1133 segmented diagnostic slides were saved at 5 $\times$  magnification. Each slide has determined regions of tumor, stroma, and rest, as well as a list of all selected TILs. Based on this information four groups of TILs densities were calculated: in stroma, stroma border, tumor associated stroma border, and tumor border. The features for patients with multiple slides were mean aggregated. The description of the regions is visualized in Figure 5.13. The overall TILs density in stroma was considered a baseline feature. All densities were calculated as  $\frac{\text{Number of TILs}}{\text{Area in } \mu\text{m}^2}$ . For each border region, different widths were used. Tumor border experiments included lower border widths of 10-40  $\mu\text{m}$ . Whereas stroma borders ranged between 50 and 350  $\mu\text{m}$ . Additionally, tumor associated stroma border of 125  $\mu\text{m}$  was included, since this is the optimal border found in the original paper [55]. It resulted in 20 features that were first evaluated on correlation as depicted on a heatmap Figure 5.14. There are three coherent groups visible in Figure 5.14. There is a clear link between different groups and the baseline, such as a high correlation of TILs density in stroma with TILs densities in stroma borders, which increases the bigger the border gets. And on a contrary, a lower correlation of baseline with TILs density in tumor borders. The values of pair-wise Pearson correlations in each group were compared and the columns with a correlation higher than 90% were removed. If all columns in a group displayed a correlation above 90%, the most similar column of a group was kept, which should represent a group best. The resulting features and their correlations can be seen on the right heatmap in Figure 5.14. For further comparison, features were evaluated at different prevalences. For every feature, the patients were sorted descending according to a current feature. For every prevalence in the range of 0.2 until 0.9, the patients were separated into according groups and the Kaplan Meier method was used on both of them. The Log-Rank test was applied to measure whether the two resulting event series are statistically different. The resulting p-values are visualized in Figure 5.16, both as a line plot per each prevalence, as well as a boxplot. In the boxplot, it can be seen that the median p-value of the density in 100  $\mu\text{m}$  tumor associated stroma and in 10  $\mu\text{m}$  tumor border lay higher than the other features. Those densities are also found more frequently over the statistical significance line in the line plot. Those features were

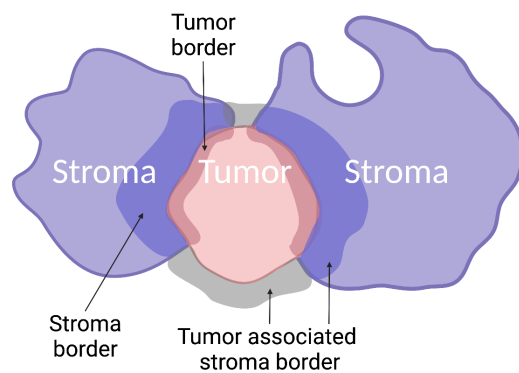


Figure 5.13: Schematic border explanation.  
Created with BioRender.com

## 5 Results & Discussion

---

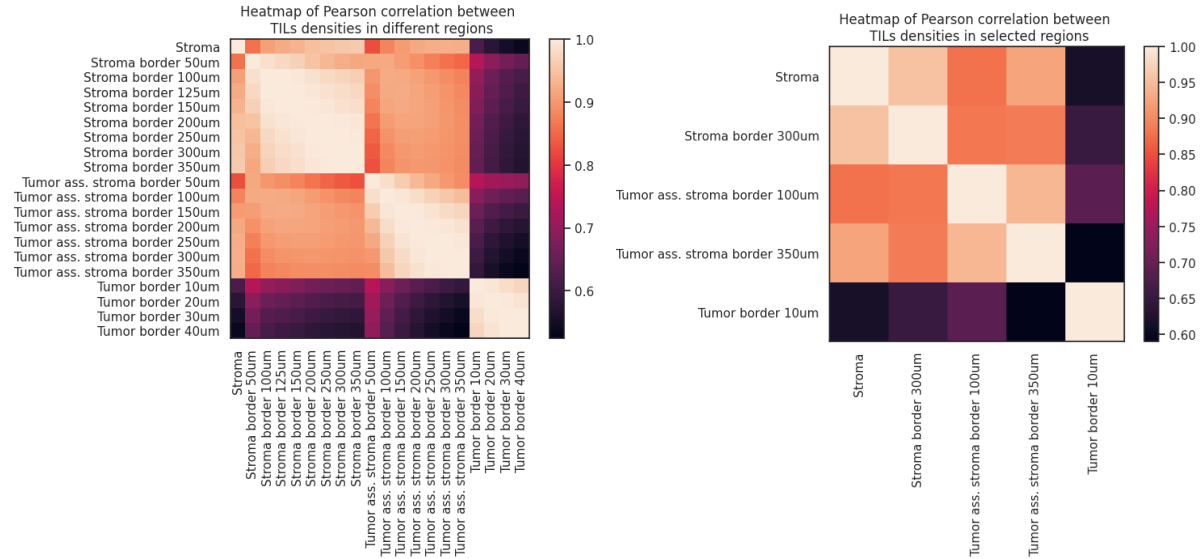


Figure 5.14: Heatmaps representing pair-wise Pearson correlation between TILs densities in different areas. Full version and condensed to group representatives.

decided to exclude. And for visibility, the remaining features were plotted again separately in Figure 5.17 with an additional boxplot depicting differences in median survival time at the same prevalence range. TILs density in tumor associated stroma achieving lower p-values in the lower prevalences. But TILs density in stroma border shows a better performance overall. It is also a feature that stays under the significance line across all prevalences. Additionally, according to the Median survival time boxplot, the median value of TILs densities in stroma border is 1.5 years higher.

By fitting the data into a Cox model, the TILs densities were divided by 100. The result revealed 0.58 concordance, 0.01 p-value, and 0.94 hazard ratio. That means that the coefficient is negative (-0.06) which supports the assumption that the high level of TILs plays a role in longer survival probability. For the TILs density in stroma border, the result is identical: 0.58 concordance, 0.01 p-value, and 0.94 hazard ratio. And TILs density in tumor associated stroma reaches 0.59 concordance, 0.01 p-value, and 0.88 hazard ratio. Regression models generally give more reliable results with normally-distributed variables. Since the TILs densities are not normally-distributed (see Figure 5.15), the experiments were repeated with log features. The TILs densities in stroma scored 0.58 concordance, p-value 0.00064 and 0.8 hazard ratio, for TILs densities in stroma border - 0.58 concordance, p-value 0.00034 and 0.79 hazard ratio, and TILs densities in tumor associated stroma - concordance of 0.59, p-value 0.00019 and 0.78 hazard ratio. It was expected for concordance to stay indifferent since did not influence it by taking the log of all values. Whereas p-values and hazard ratios improved drastically. It is harder to explain the signal presence and meaning of log-ed features, hence we will concentrate on raw values.

## 5 Results & Discussion

---

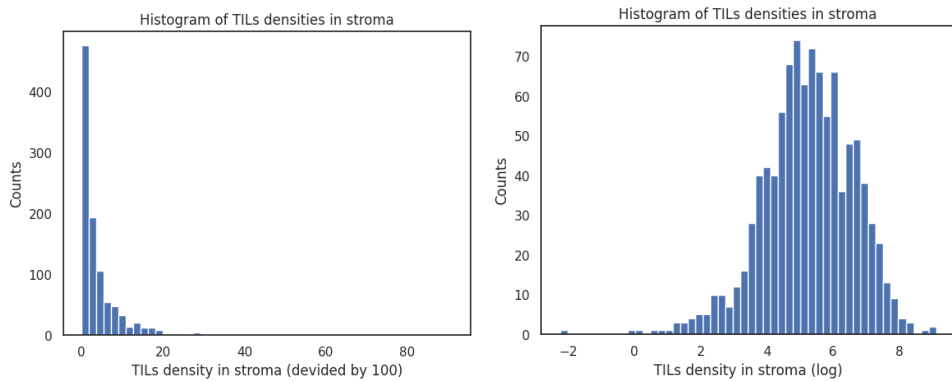


Figure 5.15: Histograms of baseline TILs density in stroma features versus its log distribution.

The Kaplan Meier curves in Figure 5.18 at most often viewed prevalences of 0.33, 0.66, and the median matched the cases when TILs density in tumor associated stroma features stratified patients better in lower range and median. Whereas at 0.66 the TILs density in stroma border scores a slightly more significant p-value.

All in all, it is not trivial to decide which feature is better and more reliable. It is clear though, that TIL density related features carry a signal in the TCGA-BRCA dataset.

## 5 Results & Discussion

---

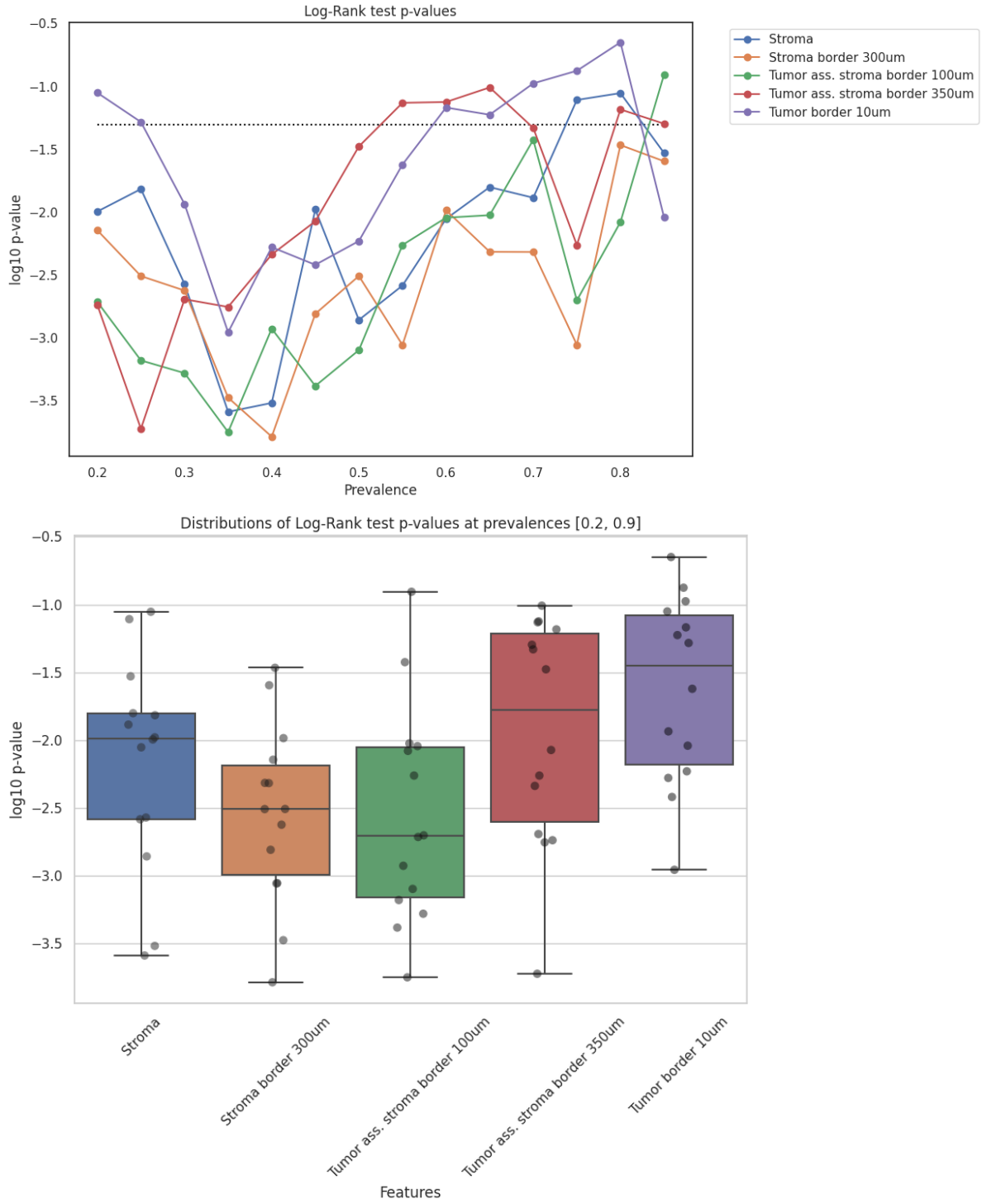


Figure 5.16: Log-Rank p-values distribution by different patient separations. The dotted line in the line plot represents the significance level of 0.05 ( $\log_{10} 0.05$ )

## 5 Results & Discussion

---

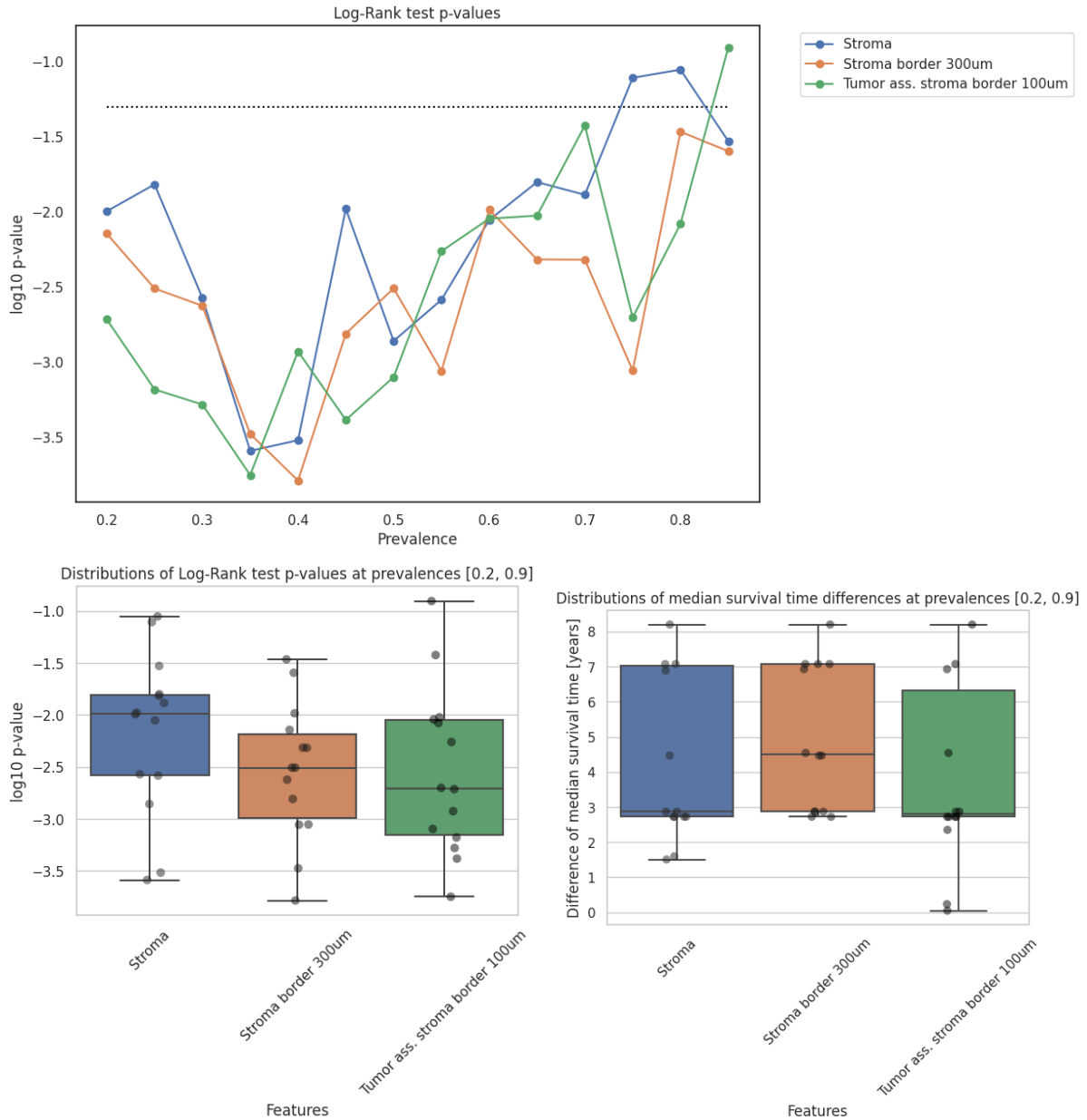


Figure 5.17: Log-Rank p-values distribution by different patient separations with an additional boxplot with median survival time differences. The dotted line in the line plot represents the significance level of 0.05 ( $\log_{10} 0.05$ )

## 5 Results & Discussion

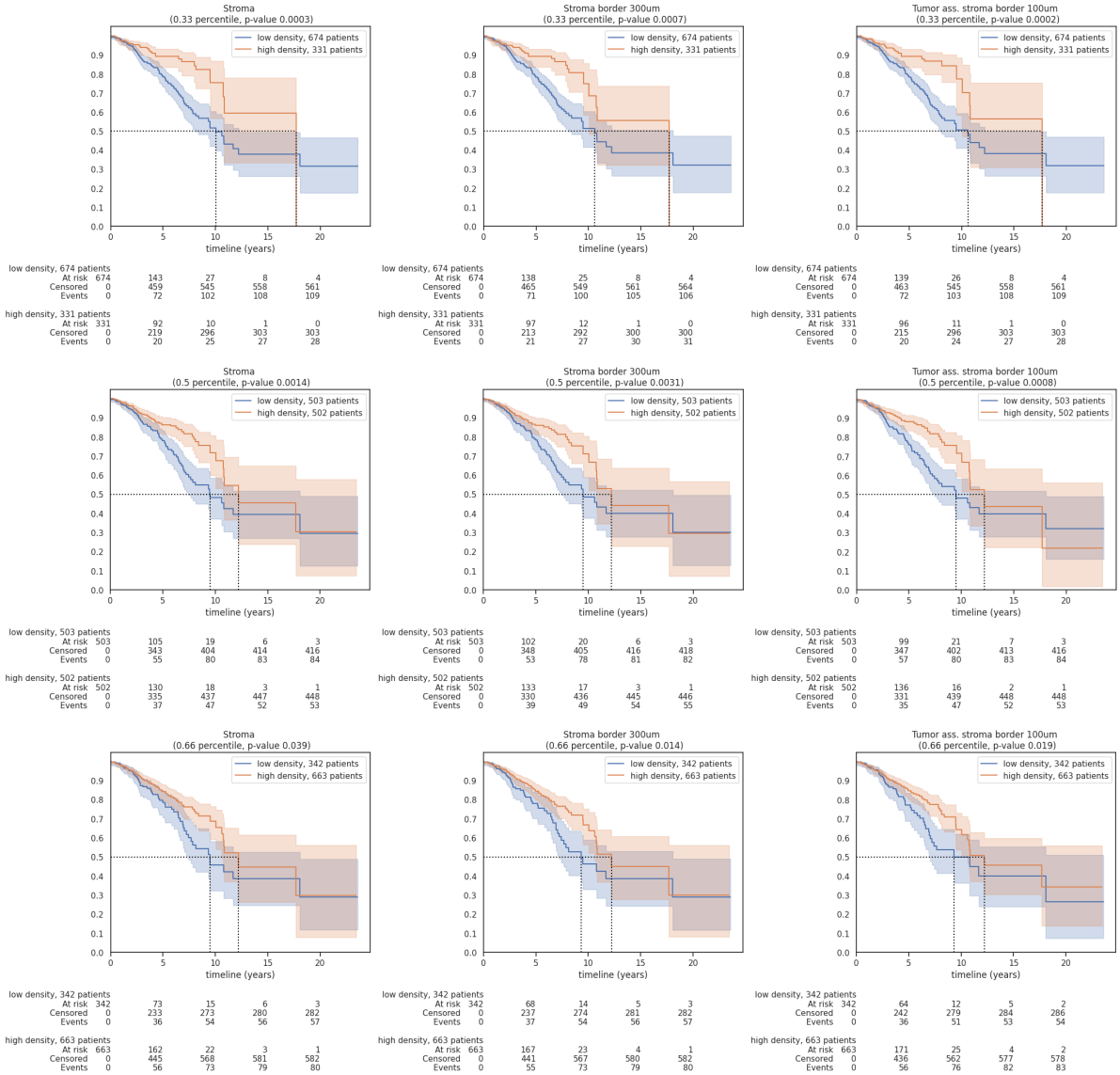


Figure 5.18: Kaplan Meier curves. Columns correspond to denisty features in: stroma, 300  $\mu\text{m}$  stroma border, 100  $\mu\text{m}$  tumor associated stroma border. Rows coorespond to following prevalences: 0.33, 0.5, and 0.66.

## 6 Conclusion

In this thesis, a new pipeline for TILs scoring in breast cancer patients was presented. The tasks of tissue segmentation and TILs detection for WSI were approached with DeepLabv3+ which is actively used in computational pathology, as well as with a novel transformer-based approach, SegFormer. As a result, the SegFormer was found to be superior in the TILs segmentation task. The analysis of TCGA-BRCA slides with the resulting models, allowed for experiments with different TILs density based features. Several of them showed the ability to successfully stratify patients at multiple prevalences. This proves a strong signal of TILs in the TCGA-BRCA dataset, which was not previously demonstrated while analyzing exclusively this publically available dataset.

As an outlook, one of the main missing prospects of this work is the absence of benchmarking with the existing challenge entries. Due to the late start of this work the submission portal was closed by the time the models were present. The TiGER challenge team that achieved the highest rank on the preliminary leaderboards for both segmentation of tissue and TILs published their approach before the challenge ended. The authors [74] trained Efficient-UNet-B0 for both tasks using Jaccard loss. The model was trained via a stratified 5-fold cross-validation framework with  $512 \times 512$  patches at  $10 \times$  magnification, with a stride of 256 pixels. Whereas for TILs segmentation, the patches of  $128 \times 128$  were extracted at  $20 \times$  magnification, with a stride of 100 pixels. The selected model with the best F1-score across each experiment on 5-fold cross-validation achieved a dice score of 0.762 for tumor segmentation, 0.718 for stroma segmentation, and 0.702 for TILs detection. The TILs score was calculated by dividing the total predicted TILs area by the stromal area and multiplying by 100. The score was further constrained to be an integer between 0 and 100. The resulting TILs scores got the highest concordance of 0.719 for predicting survival as part of a Cox proportional hazards model. Right now any of the results in this paper or any future papers of the TiGER challenge can be compared to the results in this thesis, due to the arrangement of the challenge, the reported results are based on hidden test set and internal clincal data. As long as the submission server is closed, those models and ideas need to be reimplemented. Besides benchmarking, those challenge entries can provide valuable ideas for improvements to the current pipeline. Such as applying transfer-learning, by using this model with pre-trained weights from ImageNet for tissue segmentation or an on-the-fly under-sampling approach to alleviate class imbalance of TILs segmentation task. There are also some similarities in approaches such as, similarly to this thesis, the authors [74] viewed TILs detection problem as TILs segmentation, but additionally, stain augmentation was applied. Even though the importance of the stain addition could be suspected from the tissue segmentation results, this is one of the valuable experiments that can be further performed. All in all, this thesis also provides a better understanding and test possibilities for TILs features development. Instead

---

*6 Conclusion*

of blindly submitting a value, adapting the TCGA-BRCA data set enables it to actually view the data specifics which could have helped the participants if the challenge (applicable if of course TCGA-BRCA data is not included in the hidden clinical data of the data set).

# List of Figures

1.1	Abstract scheme to visually introduce the flow of this thesis work.	2
3.1	(a) Atrous convolution, (b) ASPP augmented with Image Pooling (or Image-level features) [33]	9
3.2	The spatial pyramid pooling module of DeepLabv3 (a), the encoder-decoder structure (b) and DeepLabv3+ adaptation (c) [34]	10
3.3	DeepLabv3+ architecture. DeepLabv3 as encoder and proposed decoder structure for semantic image segmentation. [34]	10
3.4	Transformer model architecture. [63]	11
3.5	Scaled Dot-Product Attention (left). Multi-Head Attention consists of several attention layers running in parallel (right). [63]	12
3.6	SegFormer consists of two main modules: A hierarchical Transformer encoder to extract coarse and fine features; and a lightweight All-MLP decoder to directly fuse these multi-level features and predict the semantic segmentation mask. “FFN” indicates feed-forward network. (modified image [46] according to the official implementation)	13
4.1	Scheme of tasks completed in this thesis accomplitanted with the data sources and counts.	19
5.1	Confusion matrices on pixel level for DeepLabv3+, SegFormer and SegFormer with AdamW optimizer based on test set of 32 ROIs.	23
5.2	Boxplots of pixel wise calculated dice score across three datastes (TCGA-BRCA, RUMC, JB) and three segmentation labels.	24
5.3	Example of rich false positive segmentation RUMC ROI that contributes to the cases of close zero dice scores.	25
5.4	Boxplots of pixel wise calculated precision and recall across three datastes (TCGA-BRCA, RUMC, JB) and three segmentation labels.	26
5.5	Example of a slightly devalued dice score due to some annotation inaccuracies.	27
5.6	JB S_250B ROI segmentation result.	28
5.7	JB S_250B ROI segmentation result.	29
5.8	TCGA-EW-A1P4-01Z-00-DX1 ROI segmentation result.	30
5.9	Determination process for best kappa and kernel size for DeepLabv3+ (first in the first row and first in the second row), SegFormer (second in the first row), and SegFormer with AdamW (second in the second row).	32

---

*List of Figures*

---

5.10 Boxplots of dice score across three datastes (TCGA-BRCA, RUMC, JB) with maximum allowed distance between ground truth and prediction equals 10 pixels (5 $\mu\text{m}$ ). . . . .	32
5.11 Boxplots of precision and recall across three datastes (TCGA-BRCA, RUMC, JB) with maximum allowed distance between ground truth and prediction equals 10 pixels (5 $\mu\text{m}$ ). . . . .	33
5.12 TCGA-D8-A142-01Z-00-DX12 TILs prediction with DeepLabv3+, SegFormer and SegFormer, AdamW. With 0.774, 0.842 and 0.872 F1 scores accordingly. . . . .	34
5.13 Schematic border explanation. Created with BioRender.com . . . . .	35
5.14 Heatmaps representing pair-wise Pearson correlation between TILs densities in different areas. Full version and condensed to group representatives. . . . .	36
5.15 Histograms of baseline TILs density in stroma features versus its log distribution. . . . .	37
5.16 Log-Rank p-values distribution by different patient separations. The dotted line in the line plot represents the significance level of 0.05 ( $\log_{10} 0.05$ ) . . . . .	38
5.17 Log-Rank p-values distribution by different patient separations with an additional boxplot with median survival time differences. The dotted line in the line plot represents the significance level of 0.05 ( $\log_{10} 0.05$ ) . . . . .	39
5.18 Kaplan Meier curves. Columns correspond to denisty features in: stroma, 300 $\mu\text{m}$ stroma border, 100 $\mu\text{m}$ tumor associated stroma border. Rows coorespond to following prevalences: 0.33, 0.5, and 0.66. . . . .	40

# List of Tables

4.1	TiGER data overview. Sources: Cancer Genome Atlas Breast Invasive Carcinoma (TCGA-BRCA), Radboud University Medical Center (RUMC) and Jules Bordet Institute (JB). Tissue slides and ROIs refer to the segmentation images and annotations whereas TILs prefix specifies the data for TILs detection provided by the challenge. . . . .	20
4.2	Reduction of labels provided in TiGER challenge dataset. Resulting labels include three classes: Tumor (1), Stroma (2) and Rest (0) with shares of 0.312, 0.382 and 0.306. Shares were calculated by dividing the number of pixels belonging to some label by the number of the pixel in the current image and averaged over all images. . . . .	20
4.3	Data overview for TILs detection. Sources: Cancer Genome Atlas Breast Invasive Carcinoma (TCGA-BRCA), Radboud University Medical Center (RUMC) and Jules Bordet Institute (JB). Number of cells here refers to the number of bounding boxes that were assigned for lymphocytes and plasma cells, further named TILs. . . . .	21
4.4	Survival data overview. . . . .	21
5.1	Split of patients across different medical sources into train, validation, and test sets for segmentation tasks. . . . .	22
5.2	Overview of patches that were split into train, validation, and test sets for tissue segmentation. The percentages indicate the fraction of a specific conditioned group of patches to the number of all patches in the "patches" column. . . . .	22
5.3	Overview of the trained tissue segmentation models. The runtime is given for a training on one GPU NVIDIA A100 SXM4. . . . .	23
5.4	Overview of patches that were split into train, validation, and test sets for TILs segmentation. The percentages indicate the fraction of a specific conditioned group of patches to the number of all patches in the "patches" column. . . . .	31
5.5	Overview of the trained TILs segmentation models. The runtime is given for a training on one GPU NVIDIA A100 SXM4. . . . .	31

# Bibliography

- [1] B. S. Chhikara and K. Parang. "Global Cancer Statistics 2022: the trends projection analysis". In: (2022).
- [2] *Tiger - Grand Challenge*. URL: <https://tiger.grand-challenge.org/Home/>.
- [3] Q. D. Vu, S. Graham, T. Kurc, M. N. N. To, M. Shaban, T. Qaiser, N. A. Koohbanani, S. A. Khurram, J. Kalpathy-Cramer, T. Zhao, et al. "Methods for segmentation and classification of digital microscopy tissue images". In: *Frontiers in bioengineering and biotechnology* (2019), p. 53.
- [4] R. Salgado, C. Denkert, S. Demaria, N. Sirtaine, F. Klauschen, G. Pruneri, S. Wienert, G. Van den Eynden, F. L. Baehner, F. Pénault-Llorca, et al. "The evaluation of tumor-infiltrating lymphocytes (TILs) in breast cancer: recommendations by an International TILs Working Group 2014". In: *Annals of oncology* 26.2 (2015), pp. 259–271.
- [5] C. Denkert, G. von Minckwitz, S. Darb-Esfahani, B. Lederer, B. I. Heppner, K. E. Weber, J. Budczies, J. Huober, F. Klauschen, J. Furlanetto, et al. "Tumour-infiltrating lymphocytes and prognosis in different subtypes of breast cancer: a pooled analysis of 3771 patients treated with neoadjuvant therapy". In: *The lancet oncology* 19.1 (2018), pp. 40–50.
- [6] A.-V. Laenholm, G. Callagy, M. Balancin, J. Bartlett, C. Sotiriou, C. Marchio, M. Kok, C. H. Dos Anjos, and R. Salgado. "Incorporation of TILs in daily breast cancer care: how much evidence can we bear?" In: *Virchows Archiv* (2022), pp. 1–16.
- [7] M. V. Dieci, N. Radosevic-Robin, S. Fineberg, G. Van den Eynden, N. Ternes, F. Penault-Llorca, G. Pruneri, T. M. D'Alfonso, S. Demaria, C. Castaneda, et al. "Update on tumor-infiltrating lymphocytes (TILs) in breast cancer, including recommendations to assess TILs in residual disease after neoadjuvant therapy and in carcinoma in situ: a report of the International Immuno-Oncology Biomarker Working Group on Breast Cancer". In: *Seminars in cancer biology*. Vol. 52. Elsevier. 2018, pp. 16–25.
- [8] G. Gao, Z. Wang, X. Qu, and Z. Zhang. "Prognostic value of tumor-infiltrating lymphocytes in patients with triple-negative breast cancer: a systematic review and meta-analysis". In: *BMC cancer* 20.1 (2020), pp. 1–15.
- [9] M. A. Postow, M. K. Callahan, and J. D. Wolchok. "Immune checkpoint blockade in cancer therapy". In: *Journal of clinical oncology* 33.17 (2015), p. 1974.
- [10] W. Chung, H. H. Eum, H.-O. Lee, K.-M. Lee, H.-B. Lee, K.-T. Kim, H. S. Ryu, S. Kim, J. E. Lee, Y. H. Park, et al. "Single-cell RNA-seq enables comprehensive tumour and immune cell profiling in primary breast cancer". In: *Nature communications* 8.1 (2017), pp. 1–12.

## Bibliography

---

- [11] A. Schneeweiss, C. Denkert, P. A. Fasching, C. Fremd, O. Gluz, C. Kolberg-Liedtke, S. Loibl, and H.-J. Lück. "Diagnosis and therapy of triple-negative breast cancer (TNBC)–recommendations for daily routine practice". In: *Geburtshilfe und Frauenheilkunde* 79.06 (2019), pp. 605–617.
- [12] *Tiger - Grand Challenge*. URL: <https://tiger.grand-challenge.org/>.
- [13] S. Minaee, Y. Y. Boykov, F. Porikli, A. J. Plaza, N. Kehtarnavaz, and D. Terzopoulos. "Image segmentation using deep learning: A survey". In: *IEEE transactions on pattern analysis and machine intelligence* (2021).
- [14] J. Long, E. Shelhamer, and T. Darrell. "Fully convolutional networks for semantic segmentation". In: *Proceedings of the IEEE conference on computer vision and pattern recognition*. 2015, pp. 3431–3440.
- [15] H. Noh, S. Hong, and B. Han. "Learning deconvolution network for semantic segmentation". In: *Proceedings of the IEEE international conference on computer vision*. 2015, pp. 1520–1528.
- [16] I. Goodfellow, J. Pouget-Abadie, M. Mirza, B. Xu, D. Warde-Farley, S. Ozair, A. Courville, and Y. Bengio. "Generative adversarial nets". In: *Advances in neural information processing systems* 27 (2014).
- [17] D. E. Rumelhart, G. E. Hinton, and R. J. Williams. "Learning representations by back-propagating errors". In: *nature* 323.6088 (1986), pp. 533–536.
- [18] A. BenTaieb and G. Hamarneh. "Topology aware fully convolutional networks for histology gland segmentation". In: *International conference on medical image computing and computer-assisted intervention*. Springer. 2016, pp. 460–468.
- [19] V. A. Natarajan, M. S. Kumar, R. Patan, S. Kallam, and M. Y. N. Mohamed. "Segmentation of nuclei in histopathology images using fully convolutional deep neural architecture". In: *2020 International Conference on computing and information technology (ICCIT-1441)*. IEEE. 2020, pp. 1–7.
- [20] M. Amgad, A. Sarkar, C. Srinivas, R. Redman, S. Ratra, C. J. Bechert, B. C. Calhoun, K. Mrazeck, U. Kurkure, L. A. Cooper, et al. "Joint region and nucleus segmentation for characterization of tumor infiltrating lymphocytes in breast cancer". In: *Medical Imaging 2019: Digital Pathology*. Vol. 10956. SPIE. 2019, pp. 129–136.
- [21] D. A. Gutman, J. Cobb, D. Somanna, Y. Park, F. Wang, T. Kurc, J. H. Saltz, D. J. Brat, L. A. Cooper, and J. Kong. "Cancer Digital Slide Archive: an informatics resource to support integrated in silico analysis of TCGA pathology data". In: *Journal of the American Medical Informatics Association* 20.6 (2013), pp. 1091–1098.
- [22] M. Amgad, H. Elfandy, H. Hussein, L. A. Atteya, M. A. Elsebaie, L. S. Abo Elnasr, R. A. Sakr, H. S. Salem, A. F. Ismail, A. M. Saad, et al. "Structured crowdsourcing enables convolutional segmentation of histology images". In: *Bioinformatics* 35.18 (2019), pp. 3461–3467.

- [23] V. Badrinarayanan, A. Kendall, and R. Cipolla. "Segnet: A deep convolutional encoder-decoder architecture for image segmentation". In: *IEEE transactions on pattern analysis and machine intelligence* 39.12 (2017), pp. 2481–2495.
- [24] A. B. Hamida, M. Devanne, J. Weber, C. Truntzer, V. Derangère, F. Ghiringhelli, G. Forestier, and C. Wemmert. "Deep learning for colon cancer histopathological images analysis". In: *Computers in Biology and Medicine* 136 (2021), p. 104730.
- [25] O. Ronneberger, P. Fischer, and T. Brox. "U-Net: Convolutional Networks for Biomedical Image Segmentation". In: *Medical Image Computing and Computer-Assisted Intervention – MICCAI 2015*. Ed. by N. Navab, J. Hornegger, W. M. Wells, and A. F. Frangi. Cham: Springer International Publishing, 2015, pp. 234–241.
- [26] A. Lagree, M. Mohebpour, N. Meti, K. Saednia, F.-I. Lu, E. Slodkowska, S. Gandhi, E. Rakovitch, A. Shenfield, A. Sadeghi-Naini, et al. "A review and comparison of breast tumor cell nuclei segmentation performances using deep convolutional neural networks". In: *Scientific Reports* 11.1 (2021), pp. 1–11.
- [27] Z. Zeng, W. Xie, Y. Zhang, and Y. Lu. "RIC-Unet: An improved neural network based on Unet for nuclei segmentation in histology images". In: *Ieee Access* 7 (2019), pp. 21420–21428.
- [28] H. Pinckaers and G. Litjens. "Neural ordinary differential equations for semantic segmentation of individual colon glands". In: *arXiv preprint arXiv:1910.10470* (2019).
- [29] K. R. Oskal, M. Risdal, E. A. Janssen, E. S. Undersrud, and T. O. Gulsrud. "A U-net based approach to epidermal tissue segmentation in whole slide histopathological images". In: *SN Applied Sciences* 1.7 (2019), pp. 1–12.
- [30] M. E. Bagdigen and G. Bilgin. "Cell segmentation in triple-negative breast cancer histopathological images using U-Net architecture". In: *2020 28th Signal Processing and Communications Applications Conference (SIU)*. IEEE. 2020, pp. 1–4.
- [31] M. Van Rijthoven, M. Balkenhol, K. Silina, J. Van Der Laak, and F. Ciompi. "HookNet: Multi-resolution convolutional neural networks for semantic segmentation in histopathology whole-slide images". In: *Medical Image Analysis* 68 (2021), p. 101890.
- [32] L.-C. Chen, G. Papandreou, I. Kokkinos, K. Murphy, and A. L. Yuille. "Deeplab: Semantic image segmentation with deep convolutional nets, atrous convolution, and fully connected crfs". In: *IEEE transactions on pattern analysis and machine intelligence* 40.4 (2017), pp. 834–848.
- [33] L.-C. Chen, G. Papandreou, F. Schroff, and H. Adam. "Rethinking atrous convolution for semantic image segmentation". In: *arXiv preprint arXiv:1706.05587* (2017).
- [34] L.-C. Chen, Y. Zhu, G. Papandreou, F. Schroff, and H. Adam. "Encoder-decoder with atrous separable convolution for semantic image segmentation". In: *Proceedings of the European conference on computer vision (ECCV)*. 2018, pp. 801–818.

- [35] B. M. Priego-Torres, D. Sanchez-Morillo, M. A. Fernandez-Granero, and M. Garcia-Rojo. "Automatic segmentation of whole-slide H&E stained breast histopathology images using a deep convolutional neural network architecture". In: *Expert Systems With Applications* 151 (2020), p. 113387.
- [36] Y. Xie, J. Zhang, C. Shen, and Y. Xia. "Cotr: Efficiently bridging cnn and transformer for 3d medical image segmentation". In: *International conference on medical image computing and computer-assisted intervention*. Springer. 2021, pp. 171–180.
- [37] F. Visin, M. Ciccone, A. Romero, K. Kastner, K. Cho, Y. Bengio, M. Matteucci, and A. Courville. "Reseg: A recurrent neural network-based model for semantic segmentation". In: *Proceedings of the IEEE Conference on Computer Vision and Pattern Recognition Workshops*. 2016, pp. 41–48.
- [38] A. Chakravarty and J. Sivaswamy. "RACE-net: a recurrent neural network for biomedical image segmentation". In: *IEEE journal of biomedical and health informatics* 23.3 (2018), pp. 1151–1162.
- [39] M. Saha and C. Chakraborty. "Her2Net: A deep framework for semantic segmentation and classification of cell membranes and nuclei in breast cancer evaluation". In: *IEEE Transactions on Image Processing* 27.5 (2018), pp. 2189–2200.
- [40] C. Nguyen, Z. Asad, R. Deng, and Y. Huo. "Evaluating transformer-based semantic segmentation networks for pathological image segmentation". In: *Medical Imaging 2022: Image Processing*. Vol. 12032. SPIE. 2022, pp. 942–947.
- [41] Z. Liu, Y. Lin, Y. Cao, H. Hu, Y. Wei, Z. Zhang, S. Lin, and B. Guo. "Swin transformer: Hierarchical vision transformer using shifted windows". In: *Proceedings of the IEEE/CVF International Conference on Computer Vision*. 2021, pp. 10012–10022.
- [42] Z. Qian, K. Li, M. Lai, E. I. Chang, B. Wei, Y. Fan, Y. Xu, et al. "Transformer based multiple instance learning for weakly supervised histopathology image segmentation". In: *arXiv preprint arXiv:2205.08878* (2022).
- [43] A. Lin, B. Chen, J. Xu, Z. Zhang, G. Lu, and D. Zhang. "Ds-transunet: Dual swin transformer u-net for medical image segmentation". In: *IEEE Transactions on Instrumentation and Measurement* (2022).
- [44] R. Strudel, R. Garcia, I. Laptev, and C. Schmid. "Segmenter: Transformer for semantic segmentation". In: *Proceedings of the IEEE/CVF International Conference on Computer Vision*. 2021, pp. 7262–7272.
- [45] J. Chen, Y. Lu, Q. Yu, X. Luo, E. Adeli, Y. Wang, L. Lu, A. L. Yuille, and Y. Zhou. "Transunet: Transformers make strong encoders for medical image segmentation". In: *arXiv preprint arXiv:2102.04306* (2021).
- [46] E. Xie, W. Wang, Z. Yu, A. Anandkumar, J. M. Alvarez, and P. Luo. "SegFormer: Simple and efficient design for semantic segmentation with transformers". In: *Advances in Neural Information Processing Systems* 34 (2021), pp. 12077–12090.

## Bibliography

---

- [47] E. L. Kaplan and P. Meier. "Nonparametric estimation from incomplete observations". In: *Journal of the American statistical association* 53.282 (1958), pp. 457–481.
- [48] D. R. Cox. "Regression Models and Life-Tables". In: *Journal of the Royal Statistical Society: Series B (Methodological)* 34.2 (1972), pp. 187–202.
- [49] Z. Kos, E. Roblin, R. S. Kim, S. Michiels, B. D. Gallas, W. Chen, K. K. van de Vijver, S. Goel, S. Adams, S. Demaria, et al. "Pitfalls in assessing stromal tumor infiltrating lymphocytes (sTILs) in breast cancer". In: *NPJ breast cancer* 6.1 (2020), pp. 1–16.
- [50] M. Amgad, R. Salgado, and L. A. Cooper. "MuTILS: Explainable, multiresolution computational scoring of Tumor-Infiltrating Lymphocytes in breast carcinomas using clinical guidelines". In: *medRxiv* (2022).
- [51] M. Amgad, L. A. Atteya, H. Hussein, K. H. Mohammed, E. Hafiz, M. A. Elsebaie, A. M. Alhusseiny, M. A. AlMoslemany, A. M. Elmatboly, P. A. Pappalardo, et al. "Nucls: A scalable crowdsourcing, deep learning approach and dataset for nucleus classification, localization and segmentation". In: *arXiv preprint arXiv:2102.09099* (2021).
- [52] H. Le, R. Gupta, L. Hou, S. Abousamra, D. Fassler, L. Torre-Healy, R. A. Moffitt, T. Kurc, D. Samaras, R. Batiste, et al. "Utilizing automated breast cancer detection to identify spatial distributions of tumor-infiltrating lymphocytes in invasive breast cancer". In: *The American journal of pathology* 190.7 (2020), pp. 1491–1504.
- [53] Y. Bai, K. Cole, S. Martinez-Morilla, F. S. Ahmed, J. Zugazagoitia, J. Staaf, A. Bosch, A. Ehinger, E. Nimeus, J. Hartman, et al. "An Open-Source, Automated Tumor-Infiltrating Lymphocyte Algorithm for Prognosis in Triple-Negative Breast CancerMachine-Read TIL Variables in TNBC". In: *Clinical Cancer Research* 27.20 (2021), pp. 5557–5565.
- [54] A. Kapil, A. Meier, A. Shumilov, S. Haneder, H. Angell, and G. Schmidt. "Breast cancer patient stratification using domain adaptation based lymphocyte detection in HER2 stained tissue sections". In: (2021).
- [55] J. Thagaard, E. S. Stovgaard, L. G. Vognsen, S. Hauberg, A. Dahl, T. Ebstrup, J. Doré, R. E. Vincentz, R. K. Jepsen, A. Roslind, et al. "Automated quantification of stil density with h&e-based digital image analysis has prognostic potential in triple-negative breast cancers". In: *Cancers* 13.12 (2021), p. 3050.
- [56] P. Sun, J. He, X. Chao, K. Chen, Y. Xu, Q. Huang, J. Yun, M. Li, R. Luo, J. Kuang, et al. "A computational tumor-infiltrating lymphocyte assessment method comparable with visual reporting guidelines for triple-negative breast cancer". In: *EBioMedicine* 70 (2021), p. 103492.
- [57] K. E. Craven, Y. Gökm̄en-Polar, and S. S. Badve. "CIBERSORT analysis of TCGA and METABRIC identifies subgroups with better outcomes in triple negative breast cancer". In: *Scientific reports* 11.1 (2021), pp. 1–19.
- [58] D. J. Fassler, L. A. Torre-Healy, R. Gupta, A. M. Hamilton, S. Kobayashi, S. C. Van Alsten, Y. Zhang, T. Kurc, R. A. Moffitt, M. A. Troester, et al. "Spatial Characterization of Tumor-Infiltrating Lymphocytes and Breast Cancer Progression". In: *Cancers* 14.9 (2022), p. 2148.

- [59] S. Meng, L. Li, M. Zhou, W. Jiang, H. Niu, and K. Yang. "Distribution and prognostic value of tumor-infiltrating T cells in breast cancer". In: *Molecular medicine reports* 18.5 (2018), pp. 4247–4258.
- [60] V. Kotoula, K. Chatzopoulos, S. Lakis, Z. Alexopoulou, E. Timotheadou, F. Zagouri, G. Pentheroudakis, H. Gogas, E. Galani, I. Efstratiou, et al. "Tumors with high-density tumor infiltrating lymphocytes constitute a favorable entity in breast cancer: a pooled analysis of four prospective adjuvant trials". In: *Oncotarget* 7.4 (2016), p. 5074.
- [61] J. Saltz, R. Gupta, L. Hou, T. Kurc, P. Singh, V. Nguyen, D. Samaras, K. R. Shroyer, T. Zhao, R. Batiste, et al. "Spatial organization and molecular correlation of tumor-infiltrating lymphocytes using deep learning on pathology images". In: *Cell reports* 23.1 (2018), pp. 181–193.
- [62] K. He, X. Zhang, S. Ren, and J. Sun. "Deep residual learning for image recognition". In: *Proceedings of the IEEE conference on computer vision and pattern recognition*. 2016, pp. 770–778.
- [63] A. Vaswani, N. Shazeer, N. Parmar, J. Uszkoreit, L. Jones, A. N. Gomez, Ł. Kaiser, and I. Polosukhin. "Attention is all you need". In: *Advances in neural information processing systems* 30 (2017).
- [64] A. Dosovitskiy, L. Beyer, A. Kolesnikov, D. Weissenborn, X. Zhai, T. Unterthiner, M. Dehghani, M. Minderer, G. Heigold, S. Gelly, et al. "An image is worth 16x16 words: Transformers for image recognition at scale". In: *arXiv preprint arXiv:2010.11929* (2020).
- [65] N. Bodla, B. Singh, R. Chellappa, and L. S. Davis. "Soft-NMS—improving object detection with one line of code". In: *Proceedings of the IEEE international conference on computer vision*. 2017, pp. 5561–5569.
- [66] H. W. Kuhn. "The Hungarian method for the assignment problem". In: *Naval research logistics quarterly* 2.1-2 (1955), pp. 83–97.
- [67] T. G. Clark, M. J. Bradburn, S. B. Love, and D. G. Altman. "Survival analysis part I: basic concepts and first analyses". In: *British journal of cancer* 89.2 (2003), pp. 232–238.
- [68] C. Davidson-Pilon. "lifelines: survival analysis in Python". In: *Journal of Open Source Software* 4.40 (2019), p. 1317.
- [69] Y.-C. Chen. "Lecture 5: Survival Analysis". In: *STAT 425: Introduction to Nonparametric Statistics, University of Washington* (Winter 2018).
- [70] T. Therneau and E. Atkinson. "1 The concordance statistic". In: (2020).
- [71] C. Smith. *FFPE or frozen? working with human clinical samples*. Nov. 2014. URL: <https://www.biocompare.com/Editorial-Articles/168948-FFPE-or-Frozen-Working-with-Human-Clinical-Samples/>.
- [72] Choosehappy. *DOWNLOAD TCGA Digital Pathology Images (FFPE)*. Aug. 2018. URL: <http://www.andrewjanowczyk.com/download-tcga-digital-pathology-images-ffpe/>.

## Bibliography

---

- [73] M. Contributors. *MMSegmentation: OpenMMLab Semantic Segmentation Toolbox and Benchmark*. <https://github.com/open-mmlab/mmsegmentation>. 2020.
- [74] A. Shephard, M. Jahanifar, R. Wang, M. Dawood, S. Graham, K. Sidlauskas, S. A. Khurram, N. Rajpoot, and S. E. A. Raza. “TIAger: Tumor-Infiltrating Lymphocyte Scoring in Breast Cancer for the TiGER Challenge”. In: *arXiv preprint arXiv:2206.11943* (2022).